NJC

ROYAL SOCIETY OF CHEMISTRY

PAPER

View Article Online
View Journal | View Issue

Cite this: *New J. Chem.*, 2024, **48**, 11812

Understanding the second and third order nonlinear optical responses of M@$b_{66/64}Al_{12}N_{12}$: a comprehensive DFT and TD-DFT study†

Meriem Zaidi, [ab] Douniazed Hannachi, *[cd] Nahla Chaoui[a] and Henry Chermette *[e]

Materials with significant first hyperpolarizability values are essential for application in second harmonic generation to achieve frequency doubling. Therefore, ideal NLO materials must not only exhibit a substantial NLO response but also maintain transparency when exposed to laser light. In this study, we investigate two series of nanoparticles, namely M@$b_{64}Al_{12}N_{12}$ and M@$b_{66}Al_{12}N_{12}$ (M ranges from Sc to Zn). The aim is to evaluate the second and third NLO responses through DFT and TD-DFT calculations. These evaluations are performed using the CAM-B3LYP/6-311+G(d) level of theory and the sum-over-states method in the static and dynamic regime ($\lambda = \infty$, 1906, 1341, and 1064 nm). These properties are further explained by considering factors such as molecular topology, delocalization indices, Waber–Cromer radius, excitation energy, oscillator strengths, variations of dipole moment of the excited state, and one/two-photon resonance effects. The results indicate that incorporating transition metals into $Al_{12}N_{12}$ substantially increases both the first and second hyperpolarizability. The delocalization index values reveal a higher degree of electron delocalization between the transition metal and nitrogen compared to that between the transition metal and aluminum. The QTAIM analysis displays that the presence of a closed quasi-ring structure between the metal and the nanocage, combined with electron delocalization, significantly enhances the first hyperpolarizability. TD-DFT calculations suggest potential application of these compounds in deep ultraviolet laser devices due to their transparency below 200 nm. The SOS approach reveals that the most critical excited states are local excitations, characterized by high S_r, small D, and negative t values. On the other hand, in the dynamic regime, our results indicated that the values of β_{HRS}, $\beta_{SHG}(-2\omega; \omega, \omega)$ and $\gamma_{ESHG}(-2\omega; \omega, \omega, 0)$ are larger than their static counterparts. Additionally, one/two photon resonance energy, along with substantial oscillator strength, plays a pivotal role in enhancing the dynamic hyperpolarizability of the investigated nanoparticles. Our findings suggest that the increase in β^{λ} is primarily linked to two-photon resonance rather than one-photon resonance. Based on our current understanding, this study provides novel evidence that, at $\lambda = \infty$, the first hyperpolarizability of M@$b_{64/66}Al_{12}N_{12}$ is correlated with the Waber–Cromer radius of the transition metal. Additionally, in the dynamic regime, the first hyperpolarizability is correlated with the second hyperpolarizability.

Received 22nd April 2024,
Accepted 29th May 2024

DOI: 10.1039/d4nj01849d

rsc.li/njc

Introduction

Nonlinear optics (NLO) is a branch of science that deals with the interaction of materials with strong oscillating electromagnetic fields, resulting in the generation of new electromagnetic fields with different phase, amplitude, frequency, and other optical properties from the incident ones.[1,2]

When light propagates through a molecule, the valence electrons create a charge transfer relative to the atoms in the compound under the action of the induced electric field, resulting in the polarization of matter (P). The integration of first-principles methodologies with the finite-field (FF) approach is extensively utilized in the exploration of nonlinear optical responses due to

[a] *Département de chimie, Faculté des Sciences, Université Ferhat Abbas, Setif-1, Algérie, Algeria*
[b] *Laboratoire de Chimie, Ingénierie Moléculaire et Nanostructures (LCIMN), Université Ferhat Abbas, Sétif 1, Sétif 19000, Algeria*
[c] *Laboratoire d'Électrochimie, d'Ingénierie Moléculaire et de Catalyse Redox (LEIMCR), Département d'Enseignement de Base en Technologie, Faculté de Technologie, Université Ferhat Abbas, Sétif-1, Algeria. E-mail: h_douniazed@yahoo.fr*
[d] *Département de Chimie, Faculté des Sciences de la Matière, Université de Batna-1, Algeria*
[e] *Université de Lyon, Université Claude Bernard Lyon 1, Institut des Sciences Analytiques, UMR CNRS 5280, 69622 Villeurbanne Cedex, France. E-mail: Henry.chermette@univ-lyon1.fr*

† Electronic supplementary information (ESI) available. See DOI: https://doi.org/10.1039/d4nj01849d

its compatibility with diverse electronic structure techniques for the calculation of NLO coefficients.[3] In the FF approach, the energy of a system subjected to a weak and static electric field can be expressed as

$$U(E) = U(0) - \sum_i \mu_i E_i - \frac{1}{2!}\sum_{ij} \alpha_{ij} E_i E_j - \frac{1}{3!}\sum_{ijk} \beta_{ijk} E_i E_j E_k - \frac{1}{4!}\sum_{ijkl} \gamma_{ijkl} E_i E_j E_k E_l - \ldots \quad (1)$$

$U(0)$ is the is the total energy without the electric field, E_i represents the component of the electric field along the ith axis, μ_i denotes the component of the dipole moment vector, α represents the tensor of linear polarizability, and β and γ are the tensors of the first and second hyperpolarizability, respectively, which are the origins of the macroscopic 2nd and 3rd order NLO susceptibilities.

The field of nonlinear optics gained significant attention in scientific research after the discovery of second harmonic generation (SHG) by Franken *et al.* in 1961.[4] The following decades have evidenced various developments in the domain of nonlinear optics including new NLO phenomena and different new applications. These developments include for example the discovery of third harmonic generation (THG), sum or difference frequency generation, optical parametric amplification and optical parametric oscillation. These phenomena have led to the evolution of new technologies such as ultrafast lasers,[5,6] nonlinear microscopy,[7] and nonlinear optical switching.[5,6,8] Furthermore, nonlinear optical materials have great potential applications in different fields such as optoelectronics,[9,10] photonics,[11] optical computing, optical communications,[12,13] holographic imaging, dynamic image processing, *etc.*[14,15] In this regard, several strategies for tuning the NLO response of materials have been suggested: for example, reinforcing push–pull effects,[16–19] designing octupolar compounds[20,21] and asymmetric coordination complexes[22–24] introducing diffuse excess electrons,[25–28] using multi-decker sandwich clusters,[29,30] designing metal organic frameworks,[31] and so forth.

Among the many strategies reported in the literature, recent theoretical investigations have revealed that introducing excess electrons into different structures can result in a considerably large first hyperpolarizability. This effect is often observed when a metal atom (such as alkali metals, transition metals, alkaline earth metals and superalkalis) is doped into various structures (mostly the nanocages).[32–34] In recent years, significant efforts have been devoted to the study of hybrid or heterofullerene structures of group II–VI and III–V ($Al_{12}N_{12}$, $Al_{12}P_{12}$, $Al_{12}N_{12}$, $B_{12}N_{12}$, *etc.*) due to their extraordinary physicochemical properties, which include chemical stability, high thermal conductivity, wide energy gap and resistance to oxidation.[35,36] Niu *et al.* observed that alkali metal doping at various positions (b_{64} and r_6) of $Al_{12}N_{12}$ nanocages lowered the energy gap, leading to an enhancement in the nonlinear optical response of $Al_{12}N_{12}$. Let us remember that b_{64} nomenclature means above the bond between a 6 atom ring and a 4 atom ring, and r_6 means above the center of a 6 atom ring. The highest first hyperpolarizability was observed for $Li@r_6Al_{12}N_{12}$.[37] The results of Shakerzadeh *et al.* demonstrate that the structural and optoelectronic properties of $Be_{12}O_{12}$ and $Mg_{12}O_{12}$ are strongly influenced by their interaction with alkali metals. Additionally, exohedral doping resulted in larger nonlinear optical (NLO) responses than encapsulated doping for these metal oxide nanoclusters.[38] Furthermore, the same group observed that the optoelectronic nitride nanoclusters exhibit a remarkable NLO response compared to their corresponding carbides.[39,40]

On the other hand, Gilani *et al.* conducted exohedral and endohedral doping of copper on $Al_{12}N_{12}$ nanocages and concluded that $Cu@r_6Al_{12}N_{12}$ exhibited higher nonlinear optical responses compared to $Cu@b_{66}$, $Cu@b_{64}$ and Cu@endo[41] (r_4 means above the center of a 4-atom ring). According to Arshad *et al.*,[34,42] the exohedral doping of first-row transition metals at various sites (@: b_{64}, b_{66}, r_6, and r_4) on the $Al_{12}N_{12}$ and $B_{12}N_{12}$ nanocage resulted in the highest NLO response, with $Cu@r_6Al_{12}N_{12}$ showing the most significant first hyperpolarizability (b_{66} signifies a bond shared between two hexagonal rings). Additionally, it was shown that the $r_4Al_{12}N_{12}$ structure is thermodynamically less stable than $b_{64}Al_{12}N_{12}$.[42] Similarly, Irshad *et al.* performed theoretical studies on transition metal-doped $B_{12}P_{12}$ nanoclusters and observed that the first hyperpolarizability of $Sc@r_4B_{12}P_{12}$ was remarkably enhanced up to 4.4×10^4 a.u. Furthermore, $Sc@r_4B_{12}P_{12}$ and $Sc@r_6B_{12}P_{12}$ exhibited the highest values for the electro-optical Pockels effect (EOPE) and second harmonic generation (SHG), respectively.[43]

In this paper, with the objective of achieving a more comprehensive understanding of the second- and third-order nonlinear optical characteristics present in $M@Al_{12}N_{12}$ (where M spans from Sc to Zn), we conduct QTAIM, DFT, and TD-DFT calculations. These calculations are employed to investigate the electronic geometries, excited state properties, and NLO responses of two series of nanocages: $M@b_{64}Al_{12}N_{12}$ and $M@b_{66}Al_{12}N_{12}$. Key focal points encompass (i) scrutinizing the evolution of both linear and nonlinear optical properties as they relate to frequency intensity (ω = 0, 0.0239, 0.0340 and 0.0428 a.u.), (ii) evaluating the implications of transition metal atoms for these properties, and (iii) drawing insightful comparisons between $M@b_{64}Al_{12}N_{12}$ and $M@b_{66}Al_{12}N_{12}$ (we will use $M@b_{64}$ and $M@b_{66}$ in the following to shorten the typing).

The present paper is organized as follows: First, some computational details and definitions are given; next, the quantum theory of atoms in molecules (QTAIM) is analysed and delocalization indices (DI) are calculated; then, absorption spectra are discussed; in the following part, the static and dynamic NLO parameters of the doped nanocage are calculated; finally the sum-over-states method (SOS) is studied; the paper ends with some concluding remarks.

Computational methodology

The density functional theory (DFT) and time-dependent DFT (TD-DFT) calculations are performed by means of Gaussian 16

software.[44] The starting point for this computational study was the optimized structures of two nanoparticle series, specifically $M@b_{64}Al_{12}N_{12}$ and $M@b_{66}Al_{12}N_{12}$, where M ranges from Sc to Zn, previously achieved by Arshad and co-workers.[42]

The NLO response and the absorption spectra of all the studied nanoparticles were calculated at CAM-B3LYP[45] with the 6-311+G(d) basis set. CAM-B3LYP is a long-range corrected functional developed to handle the inaccuracies of the non-Coulomb part of the exchange functional at long distances. On the other hand, the Amsterdam density functional (ADF2017) software was used to perform topological analysis of the electron density at bond critical points, utilizing the concept of Bader's atoms in molecules (AIM) theory.[46–49]

The first hyperpolarizability is given as follows:

$$\langle\beta\rangle = \sqrt[2]{\beta_x^2 + \beta_y^2 + \beta_z^2} \quad (2)$$

The components of the first hyperpolarizability are represented as

$$\beta_x = \beta_{xxx} + \beta_{xyy} + \beta_{xzz} \quad (3)$$

$$\beta_y = \beta_{yyy} + \beta_{xxy} + \beta_{yzz} \quad (4)$$

$$\beta_z = \beta_{zzz} + \beta_{zyy} + \beta_{xxz} \quad (5)$$

The total magnitude of γ is estimated as[3,50,51]

$$\gamma = \sqrt{\gamma_x^2 + \gamma_y^2 + \gamma_x^2} \quad (6)$$

The average second hyperpolarizability is defined as follows:

$$\langle\gamma\rangle = \frac{1}{5}\left[\gamma_{xxxx} + \gamma_{yyyy} + \gamma_{zzzz} + 2\left(\gamma_{xxyy} + \gamma_{yyzz} + \gamma_{xxzz}\right)\right] \quad (7)$$

The i components of the second hyperpolarizabilities are defined as

$$\gamma_i = \frac{1}{15}\sum_{j,k}\left(\gamma_{ijkk} + \gamma_{jkkj} + \gamma_{jkjk}\right) \quad i,j = \{x,y,z\} \quad (8)$$

On the other hand, hyper-Rayleigh scattering (HRS) is a popular experimental method used to determine the first-order hyperpolarizability (β_{HRS}). This technique involves the use of perpendicular light polarizations. β_{HRS} can be described as[24,52,53]

$$\langle\beta_{HRS}\rangle = \sqrt{\{\langle\beta_{ZZZ}{}^2\rangle + \langle\beta_{XZZ}{}^2\rangle\}} \quad (9)$$

where $\langle\beta_{ZZZ}{}^2\rangle$ and $\langle\beta_{XZZ}{}^2\rangle$ denote the orientational averages of β tensor components, which can be calculated as follows:

$$\begin{aligned}\langle\beta_{ZZZ}{}^2\rangle = {} & \frac{1}{7}\sum_{i}^{x,y,z}\beta_{iii}{}^2 + \frac{4}{35}\sum_{i\neq J}^{x,y,z}\beta_{iiJ}{}^2 + \frac{2}{35}\sum_{i\neq J}^{x,y,z}\beta_{iii}\beta_{ijj} \\ & + \frac{4}{35}\sum_{i\neq J}^{x,y,z}\beta_{jii}\beta_{ijj} + \frac{4}{35}\sum_{i\neq J}^{x,y,z}\beta_{iii}\beta_{jji} \\ & + \frac{1}{35}\sum_{i\neq J}^{x,y,z}\beta_{Jii}{}^2 + \frac{4}{105}\sum_{i\neq J\neq k}^{x,y,z}\beta_{iij}\beta_{jkk} \\ & + \frac{1}{105}\sum_{i\neq J\neq k}^{x,y,z}\beta_{jii}\beta_{jkk} + \frac{4}{105}\sum_{i\neq J\neq k}^{x,y,z}\beta_{iij}\beta_{kkj} \\ & + \frac{2}{105}\sum_{i\neq J\neq k}^{x,y,z}\beta_{ijk}{}^2 + \frac{4}{105}\sum_{i\neq J\neq k}^{x,y,z}\beta_{ijk}\beta_{jik}\end{aligned}$$

$$\begin{aligned}\langle\beta_{XZZ}{}^2\rangle = {} & \frac{1}{35}\sum_{i}^{x,y,z}\beta_{iii}{}^2 + \frac{4}{105}\sum_{i\neq J}^{x,y,z}\beta_{iii}\beta_{ijj} - \frac{2}{35}\sum_{i\neq J}^{x,y,z}\beta_{iii}\beta_{jji} \\ & + \frac{8}{105}\sum_{i\neq J}^{x,y,z}\beta_{iiJ}{}^2 + \frac{3}{35}\sum_{i\neq J}^{x,y,z}\beta_{ijj}{}^2 \\ & - \frac{2}{35}\sum_{i\neq J}^{x,y,z}\beta_{iij}\beta_{jii} + \frac{1}{35}\sum_{i\neq J\neq k}^{x,y,z}\beta_{ijj}\beta_{ikk} \\ & - \frac{2}{105}\sum_{i\neq J\neq k}^{x,y,z}\beta_{iik}\beta_{jjk} + \frac{2}{35}\sum_{i\neq J\neq k}^{x,y,z}\beta_{ijk}{}^2 \\ & - \frac{2}{105}\sum_{i\neq J\neq k}^{x,y,z}\beta_{iij}\beta_{jkk} - \frac{2}{105}\sum_{i\neq J\neq k}^{x,y,z}\beta_{ijk}\beta_{jik}\end{aligned}$$

Furthermore, the depolarization ratios (DR) provide information about the geometry of the chromophore, which is the part of the compound responsible for the nonlinear optical (NLO) response. An ideal one-dimensional system has a DR of 5, while an octupolar molecule has a DR of 1.5.

$$\mathrm{DR} = \frac{\langle\beta_{ZZZ}{}^2\rangle}{\langle\beta_{XZZ}{}^2\rangle} \quad (10)$$

The study conducted by Chołuj *et al.* demonstrates that global hybrid functionals with low HF percentage (B3LYP, PBE0) are highly effective in precisely reproducing the absolute values of two-photon-absorption strengths for donor–acceptor molecules.[54] On the other hand, long-range exchange corrections have been considered the most suitable functionals to calculate spectroscopic parameters related to linear and nonlinear optical spectroscopy, such as first- and second-hyperpolarizabilities,[55] probably because of the short amount of HF exchange in the short range part.[56] Prior studies have indicated that CAM-B3LYP, which was utilized in this study, can produce an absorption spectrum that closely resembles experimental results and has demonstrated effectiveness in calculating both static and dynamic nonlinear optical (NLO) responses.[24,43,57–61]

The electron density difference maps (EDDM) for the crucial excited states can be precisely evaluated as follows:

$$\Delta\rho(r) = \rho_{ex}(r) - \rho_{GS}(r) \quad (11)$$

$\rho_{ex}(r)$ and $\rho_{GS}(r)$ are defined as the electronic densities associated with the excited and ground states, respectively.

On the other hand, to investigate the nature of electronic excitation in compounds, an analysis of the hole–electron distribution was performed. The distributions of holes and electrons are defined as follows:[62,63]

$$\rho^{hole}(r) = \sum_{i\to a}\left(W_i^a\right)^2\varphi_i(r)\varphi_i(r) + \sum_{i\to a}\sum_{j\neq i\to a} W_i^a W_j^a \varphi_i(r)\varphi_j(r) \quad (12)$$

$$\rho^{ele}(r) = \sum_{i\to a}\left(W_i^a\right)^2\varphi_a(r)\varphi_a(r) + \sum_{i\to a}\sum_{i\to b\neq a} W_i^a W_i^b \varphi_a(r)\varphi_b(r) \quad (13)$$

where φ is the orbital wave function, W is the coefficient of excitation, i and j are the occupied orbital label, and a and b are the virtual orbital label.

The overlap distribution between the hole and the electron can be expressed as

$$S_r(r) = \sqrt{\rho^{hole}(r)\rho^{ele}(r)} \quad (14)$$

To characterize the overlapping extent of holes and electrons, the S_r index is defined as

$$S_r(\text{index}) = \int S_r(r)\mathrm{d}r \equiv \int\sqrt{\rho^{hole}(r)\rho^{ele}(r)}\mathrm{d}r \quad (15)$$

The total magnitude of charge transfer (CT) length referred to as the D_{index} is calculated as

$$D_{index} = [(D_x)^2 + (D_y)^2 + (D_z)^2]^{1/2} \quad (16)$$

The charge transfer direction (H_{CT}) can be computed as

$$H_{CT} = |H\cdot u_{CT}| \quad (17)$$

u_{CT} is the unit vector in the CT direction and the H index displays the width of the average distribution of holes and electrons.

t_{index} is used to measure the separation degree between the hole and the electron in the CT direction:

$$t_{index} = D_{index} - H_{CT} \quad (18)$$

The variations of dipole moment of the excited state with respect to the ground state in X, Y and Z directions can be simply calculated as

$$\Delta\mu = \sqrt{\Delta\mu_x{}^2 + \Delta\mu_x{}^2 + \Delta\mu_x{}^2} \quad (19)$$

$$\Delta\mu_x = -(X_{ele} - X_{hole}) \quad \Delta\mu_x = -(Y_{ele} - Y_{hole})$$

and

$$\Delta\mu_z = -(Z_{ele} - Z_{hole})$$

In our work, the crucial excited state wavefunctions have been obtained by natural transition orbitals (NTOs) in terms of ''excited particle'' to ''empty hole'' of the electronic transition density matrix. The CT indices have been determined with the MULTIWFN program.[62]

Results and discussion

QTAIM

In order to understand the nature of the bonding interaction between the transition metal (M) and the $Al_{12}N_{12}$ nanocage (Scheme S1, ESI†), we have carried out topological analysis of electron density on all doped geometries M@$Al_{12}N_{12}$ according to quantum theory of atoms in molecules (QTAIM) introduced by Bader[46–49,64] using the Amsterdam density functional (ADF17) program developed by Baerends *et al.*[65,66] In QTAIM, the critical points (in ring (RCP) or bond (BCP)) are the positions where the gradient is null and which can be classified according to the electron density (ρ) and its Laplacian ($\nabla^2(\rho)$), total electron energy density (H), kinetic electron energy density (G) and potential electron energy density (V).[49,67] The results of the calculation are listed in Table 1. Fig. 1 and Fig. S1 (ESI†) depict the molecular graphs corresponding to the M@$b_{66}Al_{12}N_{12}$ and M@$b_{64}Al_{12}N_{12}$ nanocage where the red circle indicates the ring critical point (RCP) and the green circle indicates the bond critical point (BCP).

According to our calculations, Cr@b_{66}, Mn@b_{66}, Mn@b_{64}, Fe@b_{66}, Co@b_{66}, Ni@b_{66}, Zn@b_{66} and Zn@b_{64} have one BCP that is connected to the metal. This BCP found between the transition metal (M) atom and the nitrogen atom suggests the presence of M–N bonding interactions. As shown in Table 1 and Fig. 1 and Fig. S1 (ESI†), H_{BCP} values are negative and $\nabla^2(\rho)$ are high positive values, indicating that the M–N interaction is partly covalent and partly electrostatic (the average value of $\frac{-V_{BCP}}{G_{BCP}}$ is 1.293). Exceptions are Mn and Zn aluminium nitride nanocages, in which we can observe that the BCP (M–N) bond exhibits closed-shell interaction (ionic) due to their small values of ρ_{BCP} (less than 0.1) and large positive value of $\nabla^2\rho_{BCP}$.

On the other hand, Fig. 1 and Fig. S1 (ESI†) clearly show that M@$b_{64}Al_{12}N_{12}$ (M: Cr, Fe, Co, Ni and Cu) and M@$b_{66}Al_{12}N_{12}$ (M: Sc, Ti and V) have two BCPs (BCP(M–N) and BCP(M–Al)) and RCP. It is found that H_{BCP}(M–N) values are negative and $\nabla^2\rho_{BCP}$(M–N) is high and positive, meaning that the M–N bonding interactions are characteristic of partially ionic and partially covalent owing to $1 < \frac{-V_{BCP}}{G_{BCP}} < 2$. The Laplacian of the electron density ($\nabla^2\rho_{BCP}$) and the local total electronic energy density (H) are negative values and $\rho_{BCP} < 0.1$ at BCP(M–Al) indicates that this bonding is mixed covalent–ionic interaction ($\frac{-V_{BCP}}{G_{BCP}}$ on M–Al is 1.937, 1.842, 1.576 and 1.50, where M = Fe, Co, Ni and Cu, respectively).

In the case of Sc@$b_{64}Al_{12}N_{12}$, Ti@$b_{64}Al_{12}N_{12}$ and V@$b_{64}Al_{12}N_{12}$, the existence of two BCPs between M and N can be observed, exhibiting both covalent and electrostatic characteristics ($\nabla^2\rho_{BCP} > 0$ and $H_{BCP} < 0$). $\nabla^2\rho_{BCP}$ and H_{BCP} at the second BCP between M and Al are negative, which indicates the presence of ''open shell'' (covalent) character of the coordination bonds. The degree of covalence of a chemical bond can be estimated utilizing the ratio

Table 1 QTAIM calculated values of the electron density (ρ, a.u.) and its Laplacian ($\nabla^2(\rho)$, a.u.), total electron energy density (H, a.u.), kinetic electron energy density (G, a.u.) and potential electron energy density (V, a.u.)

M		ρ	∇	G	V	H
$M@b_{64}Al_{12}N_{12}$						
Sc	BCP Sc–Al	0.039	−0.020	0.009	−0.024	−0.014
	BCP Sc–N	0.123	0.375	0.150	−0.208	−0.057
Ti	BCP Ti–Al	−5.361	−3.505	1.855	4.433	5.296
	BCP Ti–N	0.043	−0.025	0.011	−0.029	−0.017
V	BCP V–Al	0.139	0.413	0.177	−0.251	−0.073
	BCP V–N	−5.388	−2.708	2.680	4.048	3.057
Cr	RCP	0.048	−0.037	0.011	−0.033	−0.021
	BCP Cr–N	0.135	0.436	0.175	−0.242	−0.066
	BCP Cr–Al	−5.710	−2.914	2.795	4.312	3.326
Mn	BCP Mn–N	0.041	0.009	0.015	−0.029	−0.013
Fe	RCP	0.115	0.409	0.147	−0.192	−0.045
	BCP Fe–Al	0.041	−0.016	0.011	−0.027	−0.015
	BCP Fe–N	0.091	0.326	0.107	−0.134	−0.026
Co	RCP	0.043	0.012	0.017	−0.031	−0.014
	BCP Co–Al	0.043	0.004	0.016	−0.031	−0.015
	BCP Co–N	0.110	0.387	0.137	−0.179	−0.041
Ni	RCP	0.045	0.024	0.020	−0.035	−0.014
	BCP Ni–Al	0.045	0.018	0.019	−0.035	−0.015
	BCP Ni–N	0.111	0.406	0.141	−0.182	−0.040
Cu	RCP	0.048	0.058	0.028	−0.042	−0.013
	BCP Cu–Al	0.049	0.047	0.026	−0.041	−0.015
	BCP Cu–N	0.113	0.429	0.147	−0.188	−0.040
Zn	BCP Zn–N	0.050	0.069	0.031	−0.044	−0.013
$M@b_{66}Al_{12}N_{12}$						
Sc	RCP	0.036	0.029	0.016	−0.025	−0.009
	BCP Sc–N	0.113	0.336	0.132	−0.181	−0.048
	BCP Sc–Al	0.037	−0.009	0.010	−0.022	−0.012
Ti	RCP	0.035	0.046	0.018	−0.025	−0.007
	BCP Ti–Al	0.035	−0.0005	0.011	−0.022	−0.011
	BCP Ti–N	0.110	0.329	0.127	−0.173	−0.045
V	RCP	0.042	0.016	0.017	−0.031	−0.013
	BCP V–Al	0.042	−0.012	0.012	−0.029	−0.016
	BCP V–N	0.115	0.370	0.140	−0.188	−0.047
Cr	BCP Cr–N	0.118	0.410	0.150	−0.197	−0.047
Mn	BCP Mn–N	0.093	0.332	0.111	−0.138	−0.027
Fe	BCP Fe–N	0.111	0.391	0.139	−0.181	−0.041
Co	BCP Co–N	0.112	0.410	0.143	−0.183	−0.040
Ni	BCP Ni–N	0.114	0.439	0.151	−0.192	−0.041
Cu	BCP Cu–N	0.126	0.490	0.173	−0.224	−0.050
Zn	BCP Zn–N	0.066	0.244	0.071	−0.082	−0.010

$-V_{BCP}/G_{BCP}$. The greater its amount, the more covalent character a bond has. Our results display that the covalent character of all M–Al (where M = Sc, Ti and V) bonds is much larger compared to any other bonds $\left(\frac{-V_{BCP}}{G_{BCP}} > 2\right)$. Furthermore, for M = Sc, Ti, and V, we observe that the H_{BCP} values of the M–N and M–Al bonds for $M@b_{64}Al_{12}N_{12}$ are more negative compared to those for $M@b_{66}Al_{12}N_{12}$. This suggests that the $Sc@b_{66}$, $Ti@b_{66}$ and $V@b_{66}$ nanocages have weaker covalent bonds, which can be attributed to the presence of the RCP. The ascending sequence for the covalent character of the M–Al bond is as follows:

Cu < Ni < Co < Fe < Cr < Ti < Sc < V.

When examining the range of M elements spanning from Cr to Zn, a noteworthy observation is that the H_{BCP} values for the M–N bond within $M@b_{66}$ are akin to those found in $M@b_{64}$. However, it is important to highlight that the Cu–N bond displays a notably enhanced covalent character (H_{BCP}(Cu–N) = −0.046 a.u.) when compared to the covalency of Cr–N, Ni–N, Co–N, Fe–N, Mn–N, and Zn–N bonds, respectively (H_{BCP}(Fe–N) = H_{BCP}(Co–N) = H_{BCP}(Ni–N) = −0.041, H_{BCP}(Zn–N) = −0.010 a.u.).

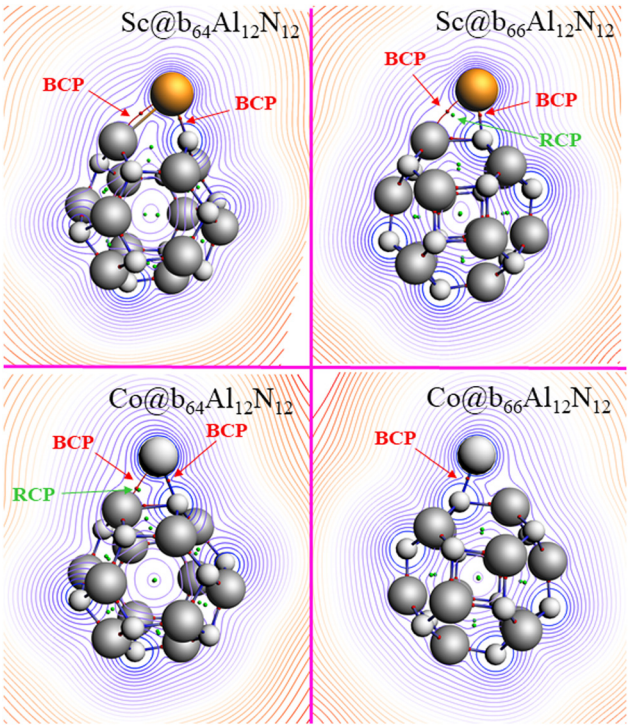

Fig. 1 Molecular topology of $Sc@b_{64}Al_{12}N_{12}$, $Sc@b_{66}Al_{12}N_{12}$, $Co@b_{64}Al_{12}N_{12}$ and $Co@b_{66}Al_{12}N_{12}$.

Delocalization indices

The concept of the "delocalization index" (DI), δ(A, B), was developed by Bader and colleagues as a method to measure electron delocalization within the framework[68,69] of the quantum theory of atoms in molecules. This index quantifies the extent of electron sharing between pairs of atoms A and B in a molecule, providing a real space measure of electron delocalization. Table 2 and Table S1 (ESI†) provide the values of δ(M, A) in $M@b_{64}Al_{12}N_{12}$ and $M@b_{66}Al_{12}N_{12}$, where A is N or Al and M is a transition metal (Scheme S1, ESI†).

In our analysis of both nanoparticles, it was noted that the delocalization index for δ(M, N) is substantially larger than that for δ(M, Al). This finding indicates a higher degree of electron delocalization between the transition metal and nitrogen in

Table 2 Delocalization indices (δ(M, A), where A = N or Al) for $M@b_{64}Al_{12}N_{12}$ and $M@b_{66}Al_{12}N_{12}$

	Sc	Ti	V	Cr	Mn	Fe	Co	Ni	Cu	Zn
$M@b_{64}Al_{12}N_{12}$										
δ(M, Al1)	0.93	0.94	0.95	0.81	0.72	0.81	0.81	0.82	0.77	0.65
δ(M, N3)	1.74	1.74	1.65	1.29	1.14	1.17	1.12	1.08	1.20	0.80
$M@b_{66}Al_{12}N_{12}$										
δ(M, Al6)	0.90	0.87	0.86	0.84	0.74	0.85	0.83	0.83	0.79	0.66
δ(M, N19)	1.58	1.46	1.41	1.28	1.14	1.18	1.12	1.10	1.19	0.80

comparison to the electron delocalization between the transition metal and aluminium.

In the series of M@b_{64} nanoparticles, where M represents Sc, Ti, V, and Cr, the δ(M, N) values range from 1.29 to 1.74. For the M@b_{66} compounds, these values are observed to be between 1.28 and 1.58. This range in δ(M, N) values implies a partial double-bond character in these complexes. Additionally, it is noted that M@b_{64} exhibits higher DI values compared to M@b_{66}, with a decreasing trend observed from Sc to Cr. The δ(M, Al) values for M@$b_{64/66}$ (M from Sc to Zn) fall within the range of 0.65 to 0.95. This range aligns with the expected characteristics of a donor–acceptor interaction in the M–Al bond.[70] On the other hand, it is observed that in the M@b_{64} series (where M ranges from Cr to Zn), the δ(M, N) and δ(M, Al) values closely resemble those reported for the M@b_{66} series. In the M@$b_{66/64}$ complexes, where M ranges from Sc to Cr, the δ(M, N) and δ(M, Al) values are observed to be higher than those in nanoparticles where M spans from Mn to Zn. Generally, it is noted that the DI values tend to decrease as the atomic number of the metal increases, with notable exceptions being the compounds of Mn and Cu. Furthermore, in the M@$b_{66/64}$ complexes, the observed delocalization index values are below 0.1. This low DI value confirms the lack of bonding interactions between the transition metal and the other atoms within the nanocage (Table S1, ESI†).

Table 3 Excitation wavelength ($\lambda_{0\to n}$, nm), oscillator strengths ($f_{0\to n}$, dimensionless), overlap ($S_r(r)$), and D and t indices (Å) associated with the $S_0 \to S_n$ transition, as calculated at CAM-B3LYP/6-311+G(d) of the studied compounds M@$b_{64/66}Al_{12}N_{12}$

M	$S_{0\to n}$	$\lambda_{0\to n}$	$f_{0\to n}$	S_r	D	t
M@$b_{64}Al_{12}N_{12}$						
Sc	$S_{0\to 5}$	766	0.009	0.795	1.085	−0.434
	$S_{0\to 13}$	463	0.144	0.578	1.187	−0.443
Ti	$S_{0\to 5}$	996	0.005	0.597	0.628	−0.455
	$S_{0\to 16}$	428	0.055	0.662	1.044	−0.749
V	$S_{0\to 5}$	822	0.001	0.596	0.442	−0.588
	$S_{0\to 15}$	407	0.116	0.757	0.896	−0.773
Cr	$S_{0\to 1}$	917	0.001	0.602	0.558	−0.736
	$S_{0\to 7}$	484	0.088	0.590	1.213	−0.664
Mn	$S_{0\to 1}$	850	0.01	0.86	0.245	−1.195
	$S_{0\to 9}$	416	0.140	0.733	1.205	−0.443
Fe	$S_{0\to 4}$	952	0.023	0.872	0.164	−1.171
	$S_{0\to 9}$	512	0.057	0.486	3.156	1.111
Co	$S_{0\to 8}$	717	<0.001	0.581	0.329	−0.633
	$S_{0\to 9}$	671	0.072	0.805	0.358	−1.001
Ni	$S_{0\to 5}$	676	0.037	0.845	0.163	−1.305
	$S_{0\to 7}$	480	0.055	0.469	3.107	1.098
Cu	$S_{0\to 1}$	591	0.076	0.726	0.667	−0.782
	$S_{0\to 2}$	468	0.057	0.489	2.952	0.927
Zn	$S_{0\to 3}$	414	0.215	0.699	0.219	−1.546
	$S_{0\to 5}$	372	0.09	0.413	3.057	1.006
M@$b_{66}Al_{12}N_{12}$						
Sc	$S_{0\to 6}$	885	0.001	0.706	0.522	−0.710
	$S_{0\to 13}$	527	0.251	0.658	1.022	−0.739
Ti	$S_{0\to 8}$	837	<0.001	0.802	0.131	−1.166
	$S_{0\to 13}$	590	0.177	0.670	0.853	−0.837
V	$S_{0\to 7}$	859	<0.001	0.544	0.514	−0.455
	$S_{0\to 12}$	495	0.075	0.594	1.841	−0.195
Cr	$S_{0\to 1}$	861	<0.001	0.601	0.536	−0.723
	$S_{0\to 7}$	495	0.097	0.579	1.409	−0.411
Mn	$S_{0\to 1}$	845	0.011	0.858	0.332	−1.199
	$S_{0\to 8}$	424	0.118	0.771	1.011	−0.542
Fe	$S_{0\to 4}$	866	0.022	0.848	0.213	−1.111
	$S_{0\to 9}$	513	0.05	0.439	3.305	1.354
Co	$S_{0\to 7}$	804	0.031	0.856	0.134	−1.170
	$S_{0\to 9}$	510	0.049	0.438	3.214	1.260
Ni	$S_{0\to 5}$	649	0.068	0.803	0.400	−0.940
	$S_{0\to 7}$	500	0.056	0.444	3.184	1.221
Cu	$S_{0\to 1}$	622	0.077	0.711	0.689	−0.701
	$S_{0\to 2}$	491	0.053	0.424	3.085	1.128
Zn	$S_{0\to 3}$	427	0.197	0.694	0.233	−1.505
	$S_{0\to 5}$	387	0.076	0.386	2.936	0.940

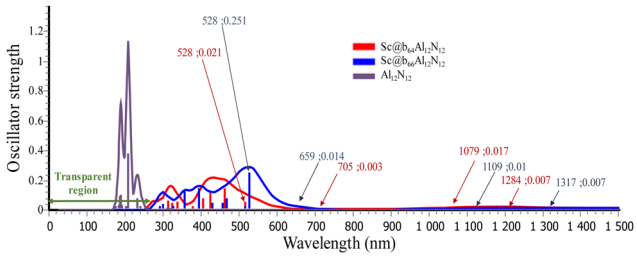

Fig. 2 Calculated UV-vis absorption spectra of $Al_{12}N_{12}$ and Sc@$b_{64/66}$-$Al_{12}N_{12}$.

Electronic spectra: UV-vis spectra and excited states

In order to achieve a more comprehensive understanding of the underlying source of nonlinear optical (NLO) properties, TD-DFT calculations were performed on the studied complexes. Table S1 (ESI†) and Table 3 summarize the spectroscopic parameters of crucial electronic transitions, including absorption wavelengths ($\lambda_{0\to n}$), oscillator strengths ($f_{0\to n}$), transition dipole moment ($\Delta\mu_{0\to n}$), overlap ($S_r(r)$), and D and t indices.

Materials that exhibit large first hyperpolarizability values are primarily employed for second harmonic generation (SHG) to double the frequency (2ω). It should be emphasized that the excellent NLO materials should not only have a large NLO response but also possess transparency under the laser light used.[71] For this objective, the ultraviolet-visible-infrared (UV-VIS-NIR) absorption spectrum of the lowest-energy $Al_{12}N_{12}$ and M@$Al_{12}N_{12}$ (M = Sc to Zn, b_{64} and b_{66}) is obtained and shown in Fig. 2 and Fig. S2 (ESI†). Based on the TD-DFT results (we used 120 excited states, which is sufficient for the objectives of this investigation[72,73]) it is evident that the absorption spectrum of isolated $Al_{12}N_{12}$ appears in the ultraviolet region between 170 and 300 nm. However, upon interaction with a transition metal, the absorption peaks of M@$Al_{12}N_{12}$ are red-shifted towards the visible region. It can be seen that Cr@$b_{64/66}$, Mn@$b_{64/66}$ and Cu@$b_{64/66}$ exhibit infrared (IR) transparent regions at a wavelength greater than 950 nm, indicating good transparency to infrared light. All these systems are fully transparent in the deep ultraviolet region ($\leq$200 nm). Therefore, they can be considered as potential candidates for high-performance nonlinear optical (NLO) materials in the deep ultraviolet range.

Our calculations reveal a minor red-shift in the calculated wavelength for M@$b_{66}Al_{12}N_{12}$ in comparison to M@$b_{64}Al_{12}N_{12}$ (with the exception of M = Fe). We can observe that the UV-Vis spectrum of Sc@b_{66} shows two peaks at 528 nm and 356 nm (f = 0.251, 0.121), whereas the spectrum of Sc@b_{64} displays peaks at

463 and 424 nm (f = 0.144, 0.121) and may be assigned to a mixed contribution of intra-charge transfer in the metal (ICT) and CT from the metal to nanocage (MNCT). For V@b_{64}, the absorption band appearing at 408 nm (f = 0.116) is formed by the αHOMO−1 → αLUMO+1 and βHOMO → βLUMO+2 excitation, which is regarded as a mixed ICT in the metal and MNCT transition (local transition S_r = 0.757). For V@b_{66}, the absorption band at 496 nm is formed by βHOMO → βLUMO+2 transitions which are of the MNCT (S_r = 0.594) character. For Ti@b_{64} the absorption band located at 394 nm, with a large oscillator strength (f = 0.12), is dominated by αHOMO−2 → αLUMO+3 and βHOMO → βLUMO+3, which are assigned to a mixed contribution from ICT and MNCT. As for Ti@b_{66} the βHOMO → βLUMO+2 excitation at 590 nm (f = 0.177) is ICT in the metal and of small MNCT character (Fig. S3, ESI†).

The electronic transition $S_0 \rightarrow S_1$ and $S_0 \rightarrow S_2$ of Cu@b_{66} at 622 and 492 is assigned as ICT in Cu and MNCT (CT from metal to nanocage) [αHOMO → αLUMO+1 and αHOMO → αLUMO, respectively] and the transition at 343 and 328 nm may be attributed to NMCT (CT from nanocage to metal) [βHOMO → βLUMO and βHOMO−1 → βLUMO, respectively]. We found similar results for Cu@b_{64} at 592, 468, 343 and 331 nm (see Table S2 and Fig. S3, ESI†). The absorption spectrum of Cr@$b_{64/66}Al_{12}N_{12}$ exhibits a moderate absorption band ranging from 600 to 900 nm, as well as strong absorption peaks at 490, 402, and 350 nm. These four states are traced to the electronic transitions of αHOMO−1 → αLUMO+1, βHOMO → βLUMO, αHOMO → αLUMO+3 and βHOMO → βLUMO+1 ($S_0 \rightarrow S_1$ (ICT), $S_0 \rightarrow S_7$ (MNCT), $S_0 \rightarrow S_{11}$ (MNCT) and $S_0 \rightarrow S_{16}$ (mixed contributions of ICT and MNCT), respectively).

It should be noted that the transition of M@$b_{64/66}Al_{12}N_{12}$, where M = Mn, Fe, Co and Ni, from αHOMO to αLUMO+1 primarily involves an intra-charge transfer within the metal at 850 nm (Ni@$Al_{12}N_{12}$), 952 nm (Fe@b_{64}), 866 nm (Fe@b_{66}), 671 nm (Co@b_{64}), 804 nm (Co@b_{66}) and 663 nm (for Ni@$Al_{12}N_{12}$). These absorptions show significantly high overlap index between the hole and the electron ($S_r > 0.8$), small D_{index} (from 0.1 to 0.4 Å), and negative t_{index} (≥ -1), indicating that they display the local excitation feature during electron transition. Furthermore, the electronic transition at ~500 nm is dominated by αHOMO → αLUMO, which shows the dominant electron transfer trend from metal to nanocage (for Mn@$Al_{12}N_{12}$, S_r = 0.6 and S_r = 0.4 where M = Fe, Co and Ni, (see Fig. 3, Fig. S3 and Table S2, ESI†). The energy absorption band appearing at ~400 nm (M = Mn, Fe and Co) is formed by the βHOMO → βLUMO+1, +2 excitation, which is regarded as a mixed ICT and MNCT transition. The absorption region at 320 nm for Ni@$Al_{12}N_{12}$ is created by the βHOMO → βLUMO transition. The shapes of molecular orbitals indicate that these transitions belong to NMCT, which involves charge transfer from a nanocage to Ni metal (S_r = 0.5) (Fig. S3 in ESI†).

On the other hand, Zn@$Al_{12}N_{12}$ exhibits electronic transition absorbing at ~420, ~378 and ~300 nm, and the major transitions are from HOMO → LUMO+1, HOMO → LUMO and HOMO−1 → LUMO. The molecular orbitals indicate that these transitions belong to ICT in Zn and MNCT and ICT in the nanoparticle (Fig. S3 and Table S2, ESI†).

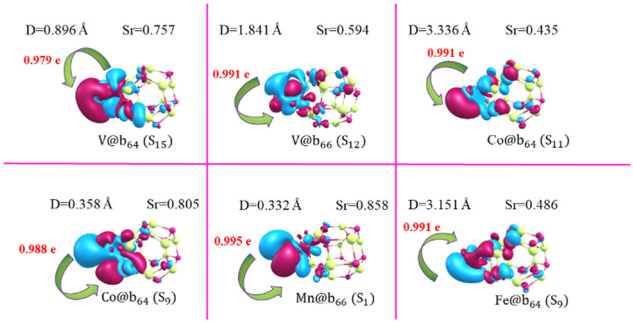

Fig. 3 Electron density difference maps of V@b_{64}, V@b_{66}, Co@b_{64}, Co@b_{66}, Mn@b_{66} and Fe@b_{64} compounds from the ground state to the crucial excited state $S_0 \rightarrow S_n$ (S_n: S_{15}, S_{12}, S_{11}, S_9, S_1 and S_9, respectively), plotted using 0.0003 a.u. isovalues (where pink and blue denote the electrons and holes, respectively).

Nonlinear optical parameters

The second and third order NLO properties of materials are closely related to various parameters, including electric dipole moment, chemical hardness, and electronic structures of compounds. Quantum chemical calculations can provide useful guidance for further experimental investigations into the second- and third-order NLO behaviour.[22–24] However, predicting the NLO properties of large nanoparticle systems using density functional theory remains a major challenge.

Nonlinear optical properties, *e.g.* first hyperpolarizability (β^{λ}_{HRS} and $\beta^{\lambda}_{SHG}(-2\omega;\ \omega,\ \omega)$), second hyperpolarizability ($\gamma^{\lambda}(-2\omega;\ \omega,\ \omega,\ 0)$) and depolarization ratios (DR^{λ}) (static ($\lambda = \infty$) as well as dynamic), for all M@$b_{64/66}Al_{12}N_{12}$ are provided in Tables 4, 5, Fig. 4 and Fig. S3 (ESI†). For calculating dynamic characteristics, three frequencies (ω) are employed, including two laser frequencies of 0.0340 a.u. (1341 nm) and 0.0428 a.u. (1064 nm) that are chosen to prevent resonance enhancement effects. Furthermore, a non-resonant frequency of 0.0239 a.u. (1906 nm) is also integrated into these systems.

First, the β^{∞}_{HRS} value of Cr@b_{64}, Mn@b_{64}, Cu@b_{64} and Zn@b_{64} is 2021, 769, 1010 and 449 a.u., which is close to 2042, 752, 1012 and 428 a.u. for Mn@b_{66}, Cu@b_{66} and Zn@b_{66}, respectively. However, the β^{∞}_{HRS} value of V@b_{66} and Ti@b_{66} is ~2 times as large as that of V@b_{64} and Ti@b_{64}, respectively, and the β^{∞}_{HRS} value of M@b_{64} is slightly larger than that of M@b_{66}, where M = Sc, Fe, Co and Ni. This suggests that the topological structure of M@$Al_{12}N_{12}$ can enhance the NLO response of materials. It can be observed that the enhancement in the first hyperpolarizability of the system can be attributed to the existence of the closed-quasi-ring (CQR) structure connecting metal and $Al_{12}N_{12}$, which includes a critical point (RCP) rather than the type of dopants (b_{64} or b_{66}). This improvement arises from the effective charge transfer between the nanocage and the metal through both the bonds and RCP, which proves to be more efficient compared to a similar charge transfer occurring in an open quasi-ring configuration. As an illustration, the larger first hyperpolarizability values observed in M@b_{66}, compared to M@b_{64} (for M = Ti and V), can be attributed to the presence of a closed-quasi-ring (CQR) in M@b_{66}, which is absent in M@b_{64}. This trend also holds

Table 4 Magnetic moment, static and dynamic first hyperpolarizability (β_{HRS}, a.u.), second harmonic generation [$\beta_{SHG}(-2\omega;\omega,\omega)$, a.u.], depolarization ratios (DR) and second-order hyperpolarizability {$\gamma(0;0,0,0)$ and $\gamma(-2\omega;\omega,\omega,0)$, $\gamma(-\omega;\omega,0,0)$, γ^{DFWM} a.u. and n_2 (cm^2 W^{-1})} of M@b$_{64}$Al$_{12}$N$_{12}$ nanoparticles

	M@b$_{64}$Al$_{12}$N$_{12}$	Sc	Ti	V	Cr	Mn	Fe	Co	Ni	Cu	Zn
	Most stable spin state	Doublet	Triplet	Quartet	Quintet	Sextet	Quintet	Quartet	Triplet	Doublet	Singlet
	Magnetic moment	10.439	10.479	10.519	10.559	10.599	10.639	10.679	10.72	10.759	10.800
$\lambda = \infty$	β_{HRS}^{∞}	6824	2844	1718	2022	769	813	873	923	1010	448
	DR^{∞}	7.614	7.769	7.812	7.325	3.725	3.779	5.085	5.550	5.584	5.462
	$\gamma(0;0,0,0)$	345 236	253 934	192 576	267 954	306 434	212 848	200 176	200 397	187 169	152 310
$\lambda = 1064$	$\beta_{SHG}(-2\omega;\omega,\omega)$	391 027	10 472	14 078	9120	20 180	47 175	10 298	12 645	17 744	2609
	β_{HRS}^{λ}	236 559	7129	7078	3640	8985	21 727	6197	5417	7316	1136
	DR^{λ}	1.339	1.454	1.883	6.937	2.565	2.038	0.661	2.474	3.224	3.941
	$\gamma(-2\omega;\omega,\omega,0)$	82 236 510	2 035 118	234 015	1 338 979	4 509 417	16 591 340	4 147 931	1 749 344	1 107 949	360 334
	$\gamma(-\omega;\omega,0,0)$	98 314 110	18 063 860	272 615	463 597	685 365	323 649	245 229	313 902	290 504	186 927
	γ^{DFWM}	125 611 201	18 657 588	286 428	820 605	2 086 359	5 783 146	1 561 147	830 217	597 430	256 268.333
	n_2 (cm^2 W^{-1})	1.04×10^{-14}	1.54×10^{-15}	2.37×10^{-17}	6.79×10^{-17}	1.72×10^{-16}	4.78×10^{-16}	1.29×10^{-16}	6.87×10^{-17}	4.94×10^{-17}	2.1219×10^{-17}
$\lambda = 1341$	$\beta_{SHG}(-2\omega;\omega,\omega)$	230 157	47 264	13 401	42 321	5938	4056	130 387	48 639	12 423	1786
	β_{HRS}^{λ}	185 510	19 823	5857	17 974	2724	2225	54 858	20 495	5108	747
	DR^{λ}	0.531	4.602	3.301	2.814	4.028	1.011	3.278	2.874	4.414	4.721
	$\gamma(-2\omega;\omega,\omega,0)$	52 964 740	2 793 484	2 078 111	7 755 519	880 009	986 328	29 036 070	6 279 438	777 884	237 633
	$\gamma(-\omega;\omega,0,0)$	65 946 960	502 537	836 282	360 031	441 008	206 335	255 234	258 541	241 221	171 978
	γ^{DFWM}	83 486 794	1 349 053	1 464 793	2 855 886	632 199	464 161	9 867 198	2 284 888	438 126	200 419
	n_2 (cm^2 W^{-1})	6.91×10^{-15}	1.11×10^{-16}	1.21×10^{-16}	2.36×10^{-16}	5.23×10^{-17}	3.84×10^{-17}	8.17×10^{-16}	1.89×10^{-16}	3.62×10^{-17}	1.6595×10^{-17}
$\lambda = 1906$	$\beta_{SHG}(-2\omega;\omega,\omega)$	29 663	716 168	6097	8840	6701	10 212	3446	3877	4214	1454
	β_{HRS}^{λ}	13 779	317 616	2370	3334	2899	8476	1473	1592	1709	592
	DR^{λ}	2.541	2.588	5.721	7.856	4.271	0.885	4.800	4.595	5.161	5.299
	$\gamma(-2\omega;\omega,\omega,0)$	830 340	732 872 500	271 797	468 308	735 755	2 325 355	285 028	294 109	282 428	184 297
	$\gamma(-\omega;\omega,0,0)$	3 126 709	1 330 356	211 553	305 011	355 683	221 614	221 461	181 224	211 312	160 842
	γ^{DFWM}	3 288 410	245 536 545	237 960	371 795	498 790	925 783	249 745	212 461	243 065	171 504.333
	n_2 (cm^2 W^{-1})	2.72×10^{-16}	2.03×10^{-14}	1.97×10^{-17}	3.07×10^{-17}	4.13×10^{-17}	7.66×10^{-17}	2.06×10^{-17}	1.75×10^{-17}	2.01×10^{-17}	1.4201×10^{-17}

Table 5 Magnetic moment, static and dynamic first hyperpolarizability (β_{HRS}, a.u.), second harmonic generation [$\beta_{SHG}(-2\omega; \omega, \omega)$, a.u.], depolarization ratios (DR) and second-order hyperpolarizability {$\gamma(0; 0, 0, 0)$ and $\gamma(-2\omega; \omega, \omega, 0)$, $\gamma(-\omega; \omega, 0, 0)$, γ^{DFWM} a.u. and n_2 ($cm^2\ W^{-1}$)} of $M@b_{66}Al_{12}N_{12}$ nanoparticles

	$M@b_{66}Al_{12}N_{12}$	Sc	Ti	V	Cr	Mn	Fe	Co	Ni	Cu	Zn
	Most stable spin state	Doublet	Triplet	Quartet	Quintet	Sextet	Quintet	Quartet	Triplet	Doublet	Singlet
	Magnetic moment	10.44	10.47	10.51	10.55	10.60	10.64	10.68	10.72	10.76	10.79
$\lambda = \infty$	β_{HRS}^{∞}	5857	4553	2701	2042	752	675	618	767	1012	428
	DR^{∞}	7.748	7.124	7.313	7.457	4.138	4.174	4.402	5.710	5.902	6.059
	$\gamma(0; 0, 0, 0)$	334 662	531 334	310 923	278 703	321 552	222 456	199 732	199 353	195 136	152 891
$\lambda = 1064$	$\beta_{SHG}(-2\omega; \omega, \omega)$	3 187 634	109 971	51 710	10 250	149 819	47 834	36 273	23 244	20 372	2725
	β_{HRS}^{λ}	1 550 925	55 883	20 770	4511	63 933	20 887	15 803	9860	8468	1163
	DR^{λ}	1.746	2.885	4.882	4.064	2.806	2.340	2.393	2.653	2.886	3.982
	$\gamma(-2\omega; \omega, \omega, 0)$	155 310 900	26 682 340	822 039	1 915 764	139 672 000	17 137 500	11 033 410	4 442 446	2 299 681	388 926
	$\gamma(-\omega; \omega, 0, 0)$	1 233 040	5 526 496	1 608 486	502 203	752 363	343 558	267 690	316 381	319 047	189 152
	γ^{DFWM}	52 891 786	14 243 498	1 778 858	1 047 890	47 202 512	5 981 906	3 878 916	1 730 745	1 020 562	267 830
	n_2 ($cm^2\ W^{-1}$)	4.37×10^{-15}	1.17×10^{-15}	1.47×10^{-16}	8.67×10^{-17}	3.91×10^{-15}	4.95×10^{-16}	3.21×10^{-16}	1.43×10^{-16}	8.45×10^{-17}	2.21×10^{-17}
$\lambda = 1341$	$\beta_{SHG}(-2\omega; \omega, \omega)$	6 248 106	84 759	21 823	39 096	5895	4809	3275	36 376	21 939	1764
	β_{HRS}^{λ}	2 587 374.28	49 485.370	11 263.96	16 938.99	2647.389	2435.229	1997.405	15 324.284	9025.444	718.428
	DR^{λ}	5.005	1.946	2.569	2.394	2.813	1.604	0.617	3.215	4.169	5.087
	$\gamma(-2\omega; \omega, \omega, 0)$	32 077 140 000	16 552 660	5 269 732	6 872 853	942 345	755 401	719 943	3 069 455	1 482 664	244 096
	$\gamma(-\omega; \omega, 0, 0)$	18 196 700 000	2 123 532	19 981 540	382 725	475 032	283 100	243 691	260 403	258 023	173 415
	γ^{DFWM}	2.88 × 10−10	7 463 974	21 634 476	2 580 775	681 963	460 748	417 094	1 217 103	687 199	203 816
	n_2 ($cm^2\ W^{-1}$)	2.39×10^{-12}	6.18×10^{-16}	1.79×10^{-15}	2.13×10^{-16}	5.64×10^{-17}	3.81×10^{-17}	3.45×10^{-17}	1.01×10^{-16}	5.69×10^{-17}	1.68×10^{-17}
$\lambda = 1906$	$\beta_{SHG}(-2\omega; \omega, \omega)$	8205	10 900	4135	8983	6774	108 286	3270	3244	4650	1423
	β_{HRS}^{λ}	4741	4247	1680	3419	2898	44 318	1496	1328	1870	564
	DR^{λ}	1.010	6.705	3.706	6.743	4.448	5.150	3.664	4.821	5.244	5.834
	$\gamma(-2\omega; \omega, \omega, 0)$	892 444	297 653	868 389	488 483	797 644	63 013 320	268 039	308 134	309 511	186 375
	$\gamma(-\omega; \omega, 0, 0)$	2 154 396	204 326	399 667	320 182	377 603	69 204 200	222 236	226 894	222 761	161 804
	γ^{DFWM}	2 042 844	126 432	585 489	390 108	536 300	90 134 488	245 005	263 154	260 886	172 965
	n_2 ($cm^2\ W^{-1}$)	1.69×10^{-16}	1.04×10^{-17}	4.84×10^{-17}	3.23×10^{-17}	4.44×10^{-17}	7.46×10^{-15}	2.02×10^{-17}	2.17×10^{-17}	2.16×10^{-17}	1.43×10^{-17}

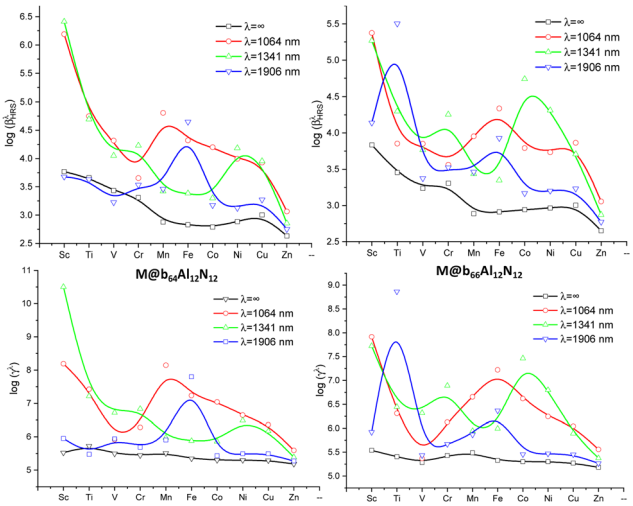

Fig. 4 Variation of the static and dynamic first hyperpolarizability (β^{λ}_{HRS}) and second hyperpolarizability (γ^{λ}) of M@$b_{64}Al_{12}N_{12}$ and M@$b_{66}Al_{12}N_{12}$ (M from Sc to Zn).

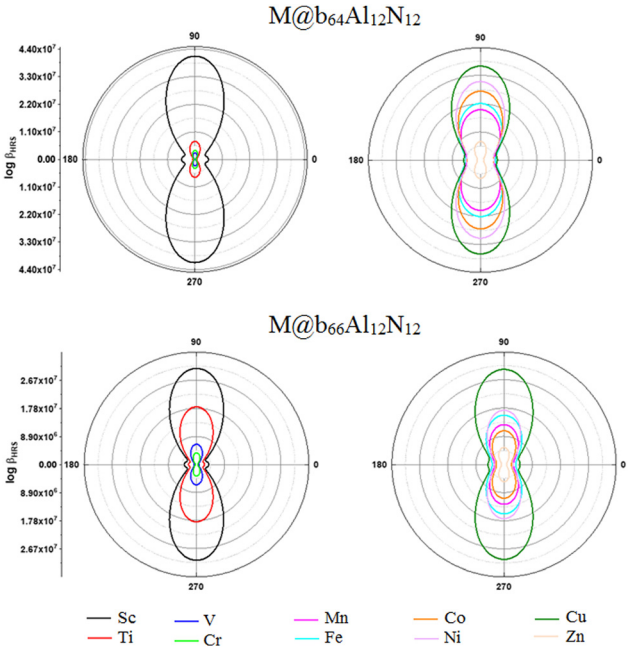

Fig. 5 Relationship between $I^{2\omega}_{\Psi V}$ and polarization angle Ψ of M@$b_{64/66}$-$Al_{12}N_{12}$.

for M = Fe, Co, Ni, and Cu, wherein a CQR is present within the M@b_{64} nanocage. Consequently, β^{∞}_{HRS}[M@b_{64}] surpasses β^{∞}_{HRS} [M@b_{66}], see Fig. 1 and Fig. S4 (ESI†) and Tables 1, 4 and 5.

Our conclusion is that the presence of a CQR structure, marked by electron delocalization, offers an explanation for the variations in first hyperpolarizability values. This elucidation effectively accounts for the distinct β^{∞}_{HRS} disparities evident between the M@b_{64} and M@b_{66} configurations (Fig. 4 and Fig. S4, ESI†).

On the other hand, the static first hyperpolarizability trends for M@$b_{66}Al_{12}N_{12}$ are similar to those observed for M@$b_{64}Al_{12}N_{12}$. Zn@$b_{64/66}Al_{12}N_{12}$ exhibits the smallest β^{∞}_{HRS} value within this series. Sc@$b_{64}Al_{12}N_{12}$ presents a large static HRS hyperpolarizability of 6824 a.u. as shown in Tables 4, 5, Fig. 4 and Fig. S4 (ESI†), which is 15 times higher than the value of Zn@$b_{64}Al_{12}N_{12}$. It is noteworthy that the $\beta^{\lambda=\infty}_{HRS}$ values of M@$b_{64}Al_{12}N_{12}$ increase as Zn < Co < Fe < Mn < Ni < Cu < Cr < V < Ti < Sc (similar to the case of the M@$b_{66}Al_{12}N_{12}$ nanocage in which the trend is Zn < Mn < Fe < Co < Ni < Cu < V < Cr < Ti < Sc).

For a deeper investigation into the underlying factors influencing the first hyperpolarizability of the compounds under study (M@$b_{64/66}Al_{12}N_{12}$ nanoparticles), we conducted polarization scans of the HRS intensity $I^{2\omega}_{\Psi V}$. The relationship between $I^{2\omega}_{\Psi V}$ and the polarization angle ψ was computed and graphed (Fig. 5 and Fig. S5, ESI†). The values of $\beta_{J=1}$ and $\beta_{J=3}$ are detailed in Table S3 (ESI†). We can observe that the DR values are sensitive to the transition metal and decrease in the following order: M@$b_{64/66}$ M: Sc ≈ Ti ≈ V ≈ Cr > Zn ≈ Cu ≈ Ni > Co > Fe > Mn. Moreover, it is worth mentioning that the nanocages M@$b_{64/66}Al_{12}N_{12}$ (M = Sc to Zn) exhibit a predominant dipolar symmetry within their nonlinear optical (NLO) responses. The DR values for these structures span from 4.1 to 7.7.

Several years ago, Hohm and Thakkar obtained a relation between the polarizability (α) and the second ionization potential (I_2) and Waber–Cromer radius (r_{WC}) of 101 elements from helium to nobelium, which can be expressed as[74]

$$\alpha = P_1 I_2^{-4} + P_2 r_{WC}^{3} I_2^{y} \quad (20)$$

Then, they obtained a fit of α roughly dominated by a linear contribution of the square root of the second ionization potential and the volume of the atom (where P_1 = 2.26, P_2 = 3.912 and y = 0.439).

In this work, we observe that the static hyperpolarizability (β_{HRS}) for M@$b_{64/66}Al_{12}N_{12}$ (M = from Sc to Zn) increases with the increase of the Waber–Cromer radius (r_{WC}) of metal (correlation coefficient equal to 0.910; see Fig. 6, Mn@$b_{64/66}$ excepted).

It is widely recognized that the measured values of the first hyperpolarizability are estimated by dispersion effects on the chromophores. Typically, the wavelength-dependent experiments are generally performed to investigate the optical resonance effects by the use of a 1064 nm (ω = 0.04282 a.u.) near infrared ray (NIR) laser. Here, the wavelengths λ = 1906, 1341 and 1064 nm were applied in calculations to compare the dispersion effect on the first hyperpolarizability of the nanocages. The second harmonic generation ($\beta^{\lambda}_{SHG}(-2\omega; \omega, \omega)$) and dynamic hyper-Rayleigh scattering response (β^{λ}_{HRS}) and its DR^{λ} of the studied nanoparticles are depicted in Tables 4 and 5. Fig. S6 in the ESI† shows an excellent correlation between β^{λ}_{HRS} and $\beta^{\lambda}_{SHG}(-2\omega; \omega, \omega)$ for the studied nanocage (R^2 ≈ 0.980). Furthermore, we can see that the dynamic β^{λ}_{HRS} values are significantly higher than the zero-frequency β^{∞}_{HRS}, except for Sc@b_{66}, Ti@b_{66} and V@b_{66} at λ = 1906 nm (see Fig. 4). As illustrated in this figure, a clear disparity in trends can be observed between the static and dynamic first

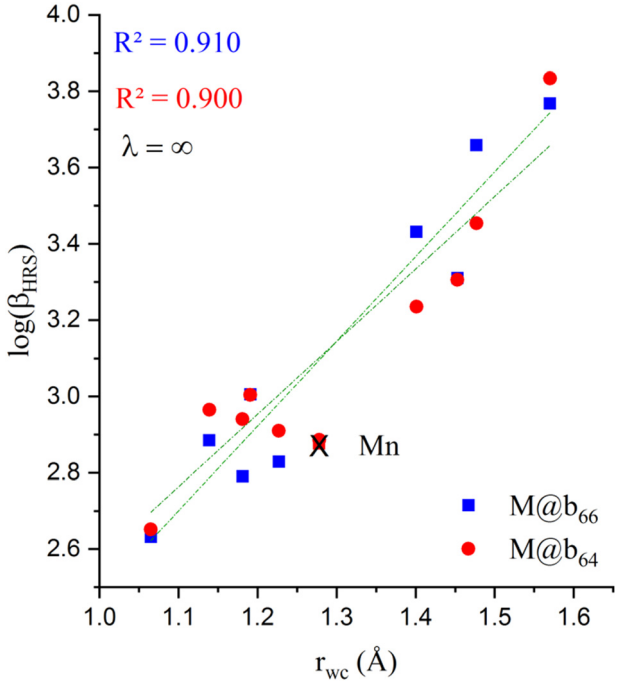

Fig. 6 Correlation between static hyper polarizability (β^{∞}_{HRS}) and Waber–Cromer radius (r_{WC}).

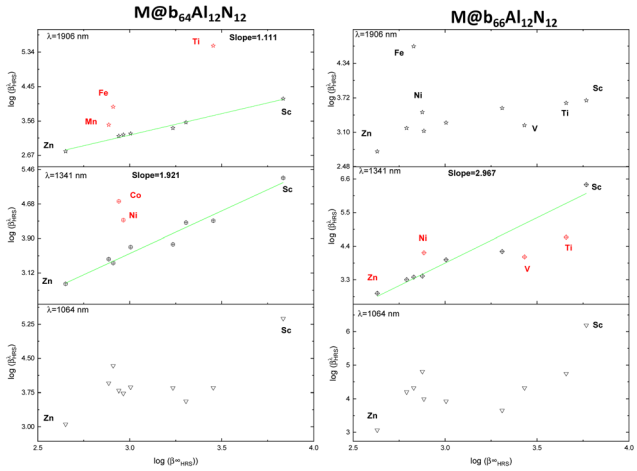

Fig. 7 The dynamic first hyperpolarizabilities of M@$b_{64/66}Al_{12}N_{12}$ (M = Sr–Zn) *versus* their static value at 1906, 1341 and 1064 nm.

hyperpolarizability values for the compounds. In simpler terms, when there is an increase in the static first hyperpolarizability value for a given nanoparticle, the dynamic value does not necessarily exhibit a similar pattern.

A careful analysis of the results obtained shows that β^{λ}_{SHG} $(-2\omega; \omega, \omega)$ of M@$b_{66}Al_{12}N_{12}$ where M = Sc, Ti, V, Mn, Co and Ni is about 8, 10, 4, 7, 4 and 2 times larger than that of M@$b_{64}Al_{12}N_{12}$, respectively, at λ = 1064 nm. For M = Cr, Fe, Cu and Zn, we note that β^{1064}_{SHG}[M@b_{64}] ≈ β^{1906}_{SHG}[M@b_{66}]. At λ = 1906 nm, the $\beta_{SHG}(-2\omega; \omega, \omega)$ response values of M@$b_{64}Al_{12}N_{12}$ decrease in the order Ti > Sc > Fe > Cr > Mn > V > Cu > Ni > Co > Zn (for M@$b_{66}Al_{12}N_{12}$ the variation of β_{SHG} takes the trend Fe > Ti > Cr > Sc > Mn > V > Co > Ni > Cu > Zn).

Regarding the HRS hyperpolarizability (Fig. 7), the static first hyperpolarizability of each nanoparticle is compared to their dynamic values (β^{λ}_{HRS}) at different wavelengths. The graph shows that for M@$b_{64}Al_{12}N_{12}$ at wavelengths of λ = 1906 and 1341 nm, a good linear relationship is observed, with a slope of 1.111 (R^2 = 0.985) and 1.921 (R^2 = 0.960), respectively, except for M = Ti, Fe and Mn at 1906 nm and M = Ni and Co at 1341 nm. This suggests that the frequency dispersion consistently affects this type of nanoparticle. Furthermore, the slopes obtained for M@$b_{64}Al_{12}N_{12}$ provide a correcting factor for the frequency dispersion of these nanoparticles at the corresponding wavelengths. We observed identical findings for M@$b_{66}Al_{12}N_{12}$ at λ = 1341 nm with a slope of 2.967 (R^2 = 0.942) (M = Ti, V and Ni excepted). On the other hand, at λ = 1064 nm, a significant resonance effect was observed, leading to numerical instability that disrupted the linear relationship. We noticed the same results for M@$b_{66}Al_{12}N_{12}$ at λ = 1906 nm (weak linear relationship β_{HRS} ↔ β^{1906}_{HRS}).

Regarding the dynamic depolarization ratio (DR), we observe that the nanoparticles Co@$b_{64}Al_{12}N_{12}$, Sc@$b_{64}Al_{12}N_{12}$ and Ti@$b_{64}Al_{12}N_{12}$ at a wavelength of 1064 nm, as well as {M@b_{66} (M = Sc, Ti, Mn, Fe, Co, Ni and Cu) and M@b_{64} (M = V, Mn, Fe, Ni, Cu)} and {M@b_{66} (M = Sc, Ti, Mn, Fe, Co, Ni and Cu) and M@b_{64} (M = V, Mn, Fe, Ni, Cu)} at wavelengths of 1341 nm and 1906 nm, respectively, are anticipated to display a dominant octupolar character. In contrast, the remaining compounds generally display a dipolar nature, with the exception of Sc@$b_{64/66}$, Ti@$b_{64/66}$ and Co@$b_{64/66}$ at λ = 1064 nm, Co@b_{66}, Sc@b_{64} and Fe@b_{64} at λ = 1341 and Sc@b_{66} and Fe@b_{64} at λ = 1906 nm, which possess a depolarization ratio (DR) less than 1.5 (Tables 3, 4 and Table S3, ESI†).

Frequency dispersion effects

The frequency dispersion factor (FDF^{λ}) between static and dynamic HRS hyperpolarizability[74] at a specific wavelength (λ = 1064, 1341 and 1906 nm (1.165, 0.942 and 0.65 eV)) can be expressed as the ratio of $\beta^{\lambda}_{HRS}/\beta^{\infty}_{HRS}$, as listed in Table S4 in the ESI.† As seen in this table, when moving from λ = ∞ to 1064 nm (ω = 0 to 1.165 eV), the variation in the FDF^{λ} value is more significant for Sc@$b_{64/66}Al_{12}N_{12}$, Ti@$b_{64}Al_{12}N_{12}$, Mn@b_{66}-$Al_{12}N_{12}$, Fe@$b_{66}Al_{12}N_{12}$, Co@$b_{64}Al_{12}N_{12}$, and Ni@$b_{64/66}Al_{12}N_{12}$, while it is negligible for Zn@$b_{64/66}Al_{12}N_{12}$ and moderate for the other nanoparticles (see Tables 3 and 4).

The dispersion of first hyperpolarizability increases significantly due to one-photon (two-photon) resonance when the frequency of the generated light ω (2ω) is close to the strong allowed excitation energy.

From the TD-DFT results (see Fig. S2, ESI†), the excitation energy of Sc@b_{64}: 2.34 eV, Sc@b_{66}: 2.35 eV, Ti@b_{66}: 2.39 eV, V@b_{64}: 2.32 eV and Mn@b_{66}: 2.35 eV is very close to the energy of the incident light 2ω (2.33 eV), whereas it is slightly different at 2.33 eV for Ti@b_{64}: 2.22 eV, Mn@b_{64}: 2.41 eV, Fe@b_{64}:

2.42 eV, Co@b_{64}: 2.48 eV and Cu@b_{64}: 2.09 eV, which is an indication of two-photon resonance. On the other hand, the excitation energy of Sc@b_{64}, Sc@b_{66}, Ti@b_{66}, V@b_{66} and Co@b_{64} at 1.15, 1.12, 1.11, 1.10 and 1.13 eV, respectively, indicates that these nanoparticles are close to one-photon resonance (ω = 1.165 eV).

In the case of ω = 0.924 eV, the two-photon resonance value of Sc@b_{66}, Co@b_{64} and Ni@b_{64} is 1.88, 1.83 and 1.84 eV and that of Sc@b_{64}, Co@b_{66} and Ni@b_{66} is 1.75, 1.68 and 1.91 eV, respectively. We can note that the resonance value of Sc@b_{66}, Co@b_{64} and Ni@b_{64} is the closest to the near-resonant energy of 1.847 eV and that of Sc@b_{64}, Co@b_{66} and Ni@b_{66} is the most deviated from the near-resonant energy (see Fig. S2, ESI†). On the other hand, the excitation energy values of Sc@b_{64}, Sc@b_{66} and V@b_{66} at 0.96, 0.94 and 0.92 eV (f = 0.007, 0.007 and 0.001), respectively, which correspond to one-photon resonance values, are in close proximity to the near-resonant energy of 0.924 eV, which causes resonance.

Based on Table S3 (ESI†), we can observe that the FDF^{1064} value of Ti@b_{66} and V@b_{66} is about 5 and 2 times larger than that of Ti@b_{64} and V@b_{64} and the FDF^{1341} and FDF^{1906} value of V@b_{66} and Fe@b_{66}, respectively, is higher than that of V@b_{64} and Fe@b_{64}, which can be attributed to the presence of one- and two-photon resonance at the same incident wavelengths. Except for Co@b_{64} and Co@b_{66} at 1064 nm, where FDF^{1064}[Co@b_{64}] < FDF^{1064}[Co@b_{66}], this can be ascribed to the smallest oscillator strength of Co@b_{64}. Furthermore, we notice that the FDF^{1064} value of Sc@b_{66} is ~9 times larger than that of Sc@b_{64}. This can be attributed to Sc@b_{66} having the highest oscillator strength at two-photon resonance (f = 0.251, λ = 528 nm).

On the other hand, our results revealed that the FDF^{1906} of M@$b_{64/66}Al_{12}N_{12}$ (where M = V–Cr, Ni–Zn), Sc@b_{66}, Ti@b_{66} and Co@b_{64} ranges from 0.62 to 1.8, indicating that the systems are far from the resonance region, *i.e.* off-resonance. A similar finding was obtained for Cr@b_{64} at 1064 nm and Zn@$b_{64/66}$-$Al_{12}N_{12}$ at 1341 nm.

Our results indicate that both the resonance energy value and the significant oscillator strength play a pivotal role in augmenting the FDF^{λ} (dynamic first hyperpolarizability) of the investigated nanoparticles. Additionally, we hypothesize that the augmentation of β^{λ} is primarily attributed to two-photon resonance rather than one-photon resonance.

Second hyperpolarizability

The second hyperpolarizability values for $Al_{12}N_{12}$ and M@$b_{64/66}$-$Al_{12}N_{12}$ (M = Sc to Zn) at the zero-frequency limit, as well as for frequency-dependent fields, calculated at the same level, are listed in Tables 4 and 5 and Table S5 (ESI†). As evident from the results, the values of γ(0; 0, 0, 0) exhibit sensitivity to the presence of the transition metal attached to $Al_{12}N_{12}$. There is a significant increase of approximately 8 times for Ti@b_{66}, around 5 times for Sc@$b_{64/66}$, V@b_{66} and Mn@$b_{64/66}$, roughly 4 times for Cr@$b_{64/66}$, Ti@b_{64} and Fe@b_{66}, and about 3 times for V@b_{64}, Fe@b_{64}, Co@$b_{64/66}$, Ni@$b_{64/66}$, Cu@$b_{64/66}$ and Zn@$b_{64/66}$. The ordering of the γ(0; 0, 0, 0) values for M@b_{66} is Ti > Sc > Mn > V > Cr > Fe > Co ≈ Ni > Cu > Zn, whereas for M@b_{64} it is Sc > Mn > Cr > Ti > Fe > Co ≈ Ni > V > Cu > Zn (see Fig. S4, ESI†).

The estimation of the frequency-dependent third-order nonlinear optical (NLO) response is performed using the dynamic second hyperpolarizability $\gamma(\omega)$, and the corresponding values are provided in Tables 4 and 5 and Fig. 4. It is noteworthy that the frequency-dependent second hyperpolarizability values are considerably larger than the values of $\beta^{\lambda}_{SHG}(-2\omega; \omega, \omega)$ at different dispersion frequencies. The sequence of the $\gamma(-2\omega; \omega, \omega, 0)$ values was γ (∞ nm) < γ (1906 nm) < γ (1341 nm) < γ (1064 nm) for nanoparticles Sc@b_{64}, Mn@b_{64}/b_{66}, Co@b_{66}, Ni@b_{66}, Cu@b_{64}/b_{66} and Zn@b_{64}/b_{66} and for compounds V@b_{64}/b_{66}, Cr@b_{64}/b_{66}, Co@b_{64} and Ni@b_{64}, the $\gamma(-2\omega; \omega, \omega, 0)$ values were γ (∞ nm) < γ (1906 nm) < γ (1064 nm) < γ (1341 nm). Taking M@$b_{66}Al_{12}N_{12}$ (M = Co to Zn) as an example, the γ value at 1064 nm (110 × 105, 44 × 105, 22 × 105 and 4 × 105 a.u., respectively) is evaluated to be the largest and at 1906 nm the smallest value of γ is observed (2.6 × 105, 3.08 × 105, 3.09 × 105 and 1.86 × 105 a.u.). This order indicates that third-order NLO response can be effectively enhanced when the wavelength of incident light is decreased from ∞ to 1064 nm, indicating that dispersion of optical nonlinearity reaches its highest point at 1064 nm. This observation is in agreement with the finding of Chen *et al.* for the cyclo[18]carbon system.[75] An opposite trend can be noticed for Ti@$b_{64}Al_{12}N_{12}$, where the $\gamma(-2\omega; \omega, \omega, 0)$ values are 7329 × 105 (λ = 1906) > 28 × 105 (λ = 1341 nm) > 20 × 105 (λ = 1064 nm); a similar enhanced response with increasing wavelength was observed by Naveen *et al.* in the study of transition metal doped $C_6O_6Li_6$.[76] On the other hand, we observed that Sc@b_{66} exhibits the highest ESHG value at 1341 and 1064 nm (320 771 × 105 and 1553 × 105 a.u., respectively), which is 137 000 and 464 times larger than the value in the static regime. This suggests a noteworthy correlation between the resonance energy and the second-third hyperpolarizability. A comparison between the dynamic first and second hyperpolarizability is provided in Fig. 8. The agreement between $\beta^{\lambda}_{SHG}(-2\omega; \omega, \omega)$ and $\gamma^{\lambda}(-2\omega; \omega, \omega, 0)$ values is prominently robust, with a correlation coefficient of approximately 0.92. The slope of the linear relationship, as obtained from the least-squares fitting, spans from 1.05 to 1.41 (Fig. 8), which indicates a tendency of second hyperpolarizability to overestimate the values.

The computed results for the dc-Kerr effect $\gamma(-\omega; \omega, 0, 0)$ are presented in Tables 4 and 5. Generally, for the title compounds, the dc-Kerr effect is more pronounced at a wavelength of 1064 nm compared to 1341 nm and 1906 nm. This suggests that the dc-Kerr effect can be enhanced by using a lower wavelength. However, there are exceptions. For Sc@b_{66}, V@b_{66}, and V@b_{64}, the highest dc-Kerr effect values are observed at 1341 nm, with values of 1.819×10^{10}, 1.998×10^{7} and 8.362×10^{5} a.u., respectively. For Fe@b_{66}, the highest value is at 1906 nm, with a dc-Kerr effect of 6.920×10^{8} a.u.

On the other hand, the estimation of the quadratic nonlinear refractive index is derived from the second hyperpolarizability coefficients, utilizing the following equation:[77]

$$n_2\ (\mathrm{cm^2\ W^{-1}}) = 8.28 \times 10^{-23} \gamma^{\mathrm{DFWM}}\ (\mathrm{a.u.}) \qquad (21)$$

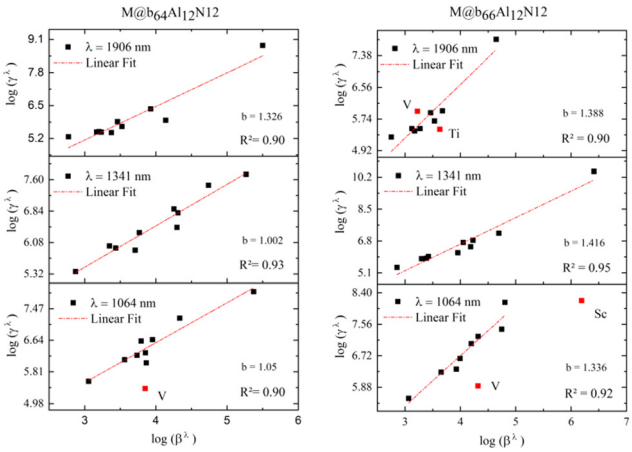

Fig. 8 Correlation between the dynamic second and third order NLO responses of M@$b_{66/64}Al_{12}N_{12}$ (M = Sc to Zn, *b* = slope).

The values for degenerate four-wave mixing (DFWM), represented as $\gamma^{\mathrm{DFWM}}(\omega) = \gamma(-\omega;\omega,-\omega,\omega)$, are calculated using the equation presented below:[78]

$$\gamma^{\mathrm{DFWM}}(-\omega;\omega,-\omega,\omega) \approx \left(\frac{1}{3}\right)\gamma(-2\omega;\omega,\omega,0) + (-\omega;\omega,0,0) - \left(\frac{1}{3}\right)\gamma(0;0,0,0) \quad (22)$$

The nanoparticles studied have displayed remarkable values of the quadratic nonlinear refractive index (n_2), as evidenced in Tables 4 and 5. Notably, the Sc@b_{66} nanoparticle exhibits the largest n_2 value of 2.39×10^{-12} cm^2 W^{-1} at 1341 nm. The n_2 values for Sc@b_{64} and V@b_{66} at 1341 nm are 6.91×10^{-15} and 1.79×10^{-15} cm^2 W^{-1}, respectively. Additionally, the Sc@$b_{64/66}$ and Tib@$b_{64/66}$ compounds also exhibit high refractive index values, falling within the range of 10^{-15} to 10^{-14} cm^2 W^{-1} at 1341 nm. On the other hand, at a wavelength of 1906 nm, the greatest n_2 value observed is 2.03×10^{-14} and 7.46×10^{-15} cm^2 W^{-1}, specifically for Ti@b_{64} and Ti@b_{66}, respectively. In general, the n_2 values for M@$b_{64/66}$ tend to decrease at the higher wavelength of 1906 nm. However, an exception is observed for Ti@$b_{64/66}$ and Fe@b_{66} particles, which exhibit a considerable enhancement in their response at this wavelength.

Controlling factors of first hyperpolarizability

A two level model is utilized to comprehend the controlling factors of the first hyperpolarizability. According to the two level model[79,80]

$$\beta_0 \propto \frac{f \times \Delta\mu}{\Delta E^3} \quad (23)$$

where $\Delta\mu$ is the difference of dipole moments between the ground state and the crucial excited state, f is the oscillator strength and ΔE is the transition energy. According to this relation, it is observed that lower excited energy (ΔE), greater dipole moment ($\Delta\mu$) and oscillator strength (f) will lead to the largest hyperpolarizability (β_0) of compounds.

To investigate the reason why some compounds exhibit large or small β_0 values, we conducted a calculation using the equation for the two-level model and compared the results with those obtained from our theoretical simulations.

As is widely recognized, the first hyperpolarizability computed using the SOS method exhibits a strong correlation with the number of excited states. Therefore, we conducted a test to investigate the convergence behaviour between the first hyperpolarizability (β_{SOS}) and the number of excited states. Fig. 9 displays the relationship between the β_{SOS} value and 120 excited states and our findings indicate that 120 excited states are adequate for achieving convergence of the β_{SOS} value.

The results presented in Fig. 10 and Table S6 (ESI†) indicate that the SOS method is capable of providing a qualitative evaluation of the first hyperpolarizability for the majority of compounds. Furthermore, the trend observed in the HRS hyperpolarizability using the SOS method is comparable to that obtained at the CAM-B3LYP/6-311+G(d) level, with only minor deviations due to the limitations of the SOS method. This consistency implies that the crucial excited states identified in Table 6 and Fig. 9 have a substantial impact on the first hyperpolarizability.

For Fe@b_{66}, Co@b_{66}, Fe@b_{64} and Ni@b_{64} the critical states correspond to the S_9, S_9, S_9 and S_7 excited states, respectively. These states show a small overlap index between the hole and the electron ($S_r \sim 0.4$), a large D_{index} (3.1–3.3 Å), and a positive t_{index} (1 to 1.35), indicating that they display the nonlocal excitation feature during electron transition. From EDDM (Fig. 9 and Fig. S3, ESI†) the crucial transition of these doped systems exhibits apparent charge transfer (CT) character from metal to $Al_{12}N_{12}$. On the other hand, for the cases of Ti@b_{64}, V@b_{64}, Mn@b_{64}, Co@b_{64}, Cu@b_{64}, Zn@b_{64}, Sc@b_{66}, Ti@b_{66}, Mn@b_{66}, Ni@b_{66}, Cu@b_{66} and *Zn*@b_{66} the dominant contribution to first hyperpolarizability values can be assigned to S_{16}, S_{15}, S_9, S_9, S_1, S_3, S_{13}, S_{13}, S_8, S_5, S_1, and S_3, respectively. Based on the analysis of the hole–electron distribution, it has been revealed that all these electronic transitions are local excitations characterized by a relatively small D_{index} (from 0.2 to 1.2 Å) a large overlap index ($S_r > 0.6$) and a negative t_{index}. This indicates that the hole and electron are in close proximity to each other (see Table S1 and Fig. S3, ESI†). For doped systems Sc@b_{64}, Cr@b_{64}, V@b_{66} and Cr@b_{66} the excited states S_{13}, S_7, S_{12}, and S_7, respectively, have large contributions to the β value, and the corresponding overlap index (and t_{index}) values of the crucial excited state are 0.578 ($t = -0.443$), 0.59 ($t = -0.664$), 0.594 ($t = -0.195$) and 0.579 Å ($t = -0.411$), respectively.

In general, a larger $f/\Delta E^3$ term can lead to larger first hyperpolarizability values, despite the constraint imposed by the $\Delta\mu$ term, which also reflects the charge transfer character of the electronic transitions. Accordingly, the large β values of Sc@b_{66} and Ti@b_{66} can be primarily ascribed to the lower electronic absorption energy paired with stronger oscillator strength (large $f/\Delta E^3$ term (0.02)). As for Zn@$b_{64/66}Al_{12}N_{12}$, its smaller β values can be attributed to its larger ΔE (2.9 eV) and smaller $\Delta\mu$ (0.4 a.u.). On the other hand, when the $f/\Delta E^3$ terms of two compounds are similar, the $\Delta\mu$ terms will have a greater

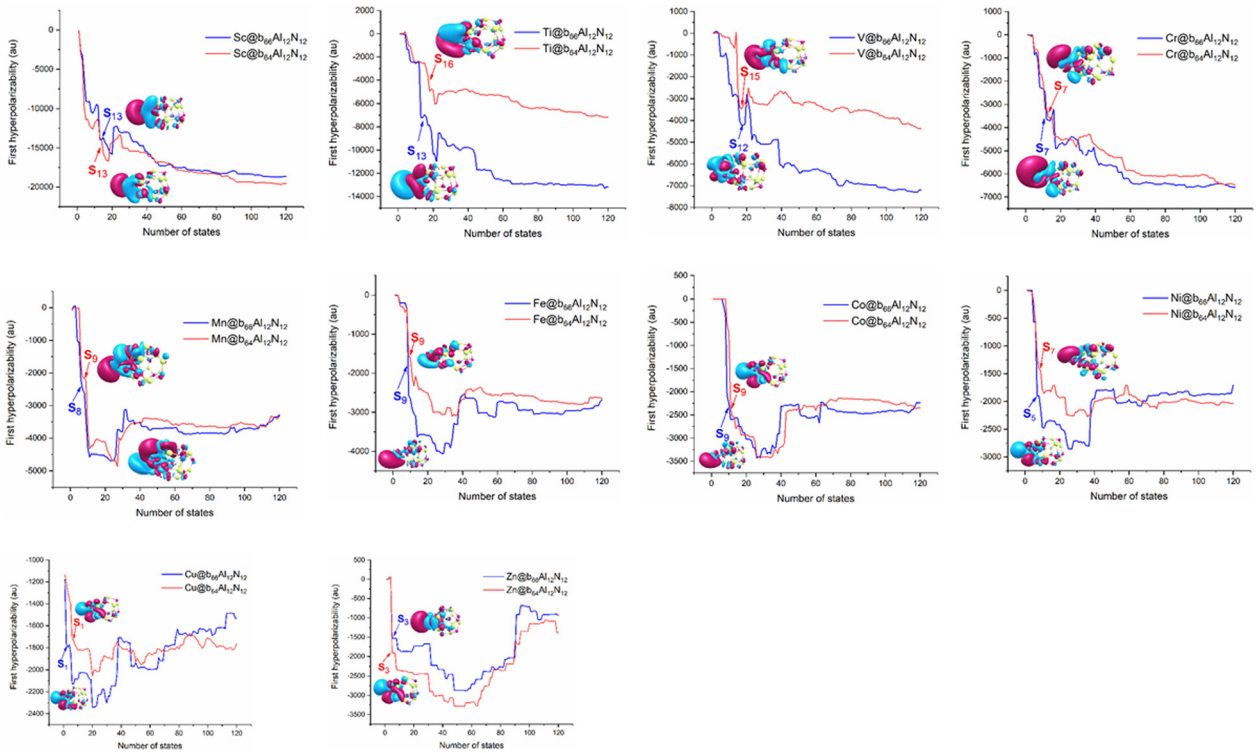

Fig. 9 Plots of static first hyperpolarizability values as computed in the SOS formalism as a function of the number of excited states for M@$b_{64/66}Al_{12}N_{12}$ (M = Sc to Zn) along with electron density difference maps, in which purple and blue colors indicate accumulation and depletion of electron density, respectively, obtained at CAM-B3LYP/6-311+G(d).

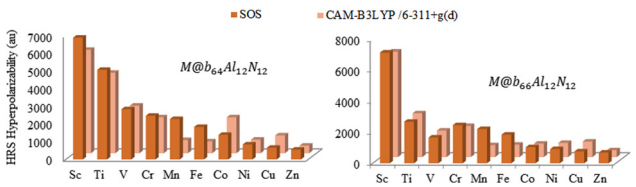

Fig. 10 Calculated static HRS-hyperpolarizability of M@$b_{64/66}Al_{12}N_{12}$ by the different methods.

influence on the resulting β values. A typical example of compounds V@b_{64} and V@b_{66} (I = 0.004, $\Delta\mu$ = 1.675 and 3.033 respectively) is illustrated here, where the significant improvement in the first hyperpolarizability value of one doped system, as compared to the other (β[V@b_{64}] < β[V@b_{66}]), is primarily attributed to the larger μ term. The same result can be achieved from Cu@b_{64} and Zn@b_{64} (I = 0.008, $\Delta\mu$ = 1.25 and 0.412 respectively). Furthermore, we observed that the β values of Cu@b_{64} and Cu@b_{66} are slightly similar to each other (see Tables 4 and 5). This can be explained by the similarities of their corresponding f, ΔE and $\Delta\mu$ terms, which result in similar $I \times \Delta\mu$ products that are proportional to the β values. The same outcome can be attained from {Cr@b_{64} and Cr@b_{66}}, {Mn@b_{64} and Mn@b_{66}} and {Zn@b_{64} and Zn@b_{66}}. It is important to note that when the I and $\Delta\mu$ terms of two compounds are similar and comparable, their f and ΔE terms play a more significant role in determining the β values than the $I \times \Delta\mu$ products. A typical case is that of Cr@b_{64} and Mn@b_{64} (I = 0.005, $I \times \Delta\mu$ = 0.012 and β[Cr@b_{64}] > β[Mn@b_{64}]) where the

Table 6 Calculated transition energy ΔE (eV), oscillator strengths (f), transition dipole moment ($\Delta\mu_{0\to n}$, a.u.) and $I = f/\Delta E^3$ of the crucial excited state ($S_0 \rightarrow S_n$)

M	S_n	$\Delta E_{0\to n}$	$f_{0\to n}$	$\Delta\mu_{0\to n}$	I	$I \times \Delta\mu_{0\to n}$
M@$b_{64}Al_{12}N_{12}$						
Sc	S_{13}	2.676	0.144	2.201	0.007	0.016
Ti	S_{16}	2.895	0.055	1.441	0.002	0.003
V	S_{15}	3.041	0.116	1.675	0.004	0.007
Cr	S_7	2.558	0.088	2.267	0.005	0.012
Mn	S_9	2.98	0.14	2.254	0.005	0.012
Fe	S_9	2.42	0.057	5.929	0.004	0.024
Co	S_9	1.848	0.072	0.672	0.011	0.008
Ni	S_7	2.582	0.055	5.838	0.003	0.019
Cu	S_1	2.095	0.076	1.25	0.008	0.010
Zn	S_3	2.994	0.215	0.412	0.008	0.003
M@$b_{66}Al_{12}N_{12}$						
Sc	S_{13}	2.35	0.251	1.888	0.020	0.036
Ti	S_{13}	2.100	0.177	1.59	0.020	0.030
V	S_{12}	2.503	0.075	3.033	0.005	0.014
Cr	S_7	2.504	0.097	2.636	0.006	0.016
Mn	S_8	2.924	0.118	1.901	0.005	0.009
Fe	S_9	2.416	0.05	6.208	0.003	0.022
Co	S_9	2.428	0.049	6.04	0.003	0.020
Ni	S_5	1.909	0.068	0.75	0.010	0.008
Cu	S_1	1.993	0.077	1.293	0.010	0.012
Zn	S_3	2.901	0.197	0.439	0.008	0.003

higher first hyperpolarizability is primarily attributed to the smaller E value of $Cr@b_{64}$.

Conclusions

In the present study, we explored the molecular topology, delocalization index, and first- and second-order hyperpolarizabilities of two nanoparticle series, specifically $M@b_{64}Al_{12}N_{12}$ and $M@b_{66}Al_{12}N_{12}$, spanning a range of transition metals from Sc to Zn, to detail their linear and nonlinear optical properties in both static and dynamic regimes.

Our results revealed a noteworthy trend: the incorporation of transition metals into the $Al_{12}N_{12}$ nanocage led to a significant increase in both the first and second hyperpolarizabilities. This enhancement in static first hyperpolarizability was linked to the presence of a ring structure bridging the M and $Al_{12}N_{12}$ nanocage. This structural pattern facilitates electron delocalization, thereby contributing to the observed increase. For instance, the $Ti@b_{66}$ nanoparticle exhibits the highest first hyperpolarizability (β^{∞}_{HRS} = 4554 a.u.) compared to $Ti@b_{64}$ (β^{∞}_{HRS} = 2844 a.u.), attributed to the presence of a closed ring structure in $Ti@b_{66}$ that was missing in $Ti@b_{64}$. According to the sum-over-states approach, the majority of crucial excited states displayed a high S_r, small D and negative t, indicating that these electronic excitations are characterized to be local excitations. Detailed UV-Vis analysis suggested that these compounds could find application in deep ultraviolet laser devices due to their transparency below 200 nm. On the other hand, in the dynamic regime, our results indicated that the values of β_{HRS}, $\beta_{SHG}(-2\omega; \omega, \omega)$ and $\gamma_{ESHG}(-2\omega; \omega, \omega, 0)$ were larger than their static counterparts. This observation emphasizes the pivotal role of one/two photon resonance energy and substantial oscillator strength in enhancing the dynamic first hyperpolarizability within the investigated nanoparticles. Moreover, our inquiry has resulted in the proposal that the enhancement of β^{λ} is predominantly motivated by the influence of two-photon resonance, rather than the conventional one-photon resonance.

The interest in new materials' picosecond and femtosecond responses spans various applications and benefits. For instance, femtosecond and picosecond lasers are instrumental in generating superhydrophilic surfaces, illustrating their significant role in material fabrication and alteration.[81] Moreover, ultrafast lasers, encompassing both picosecond and femtosecond varieties, have transformed material processing techniques, introducing novel methods for precise cutting, engraving, and drilling.[82] Additionally, treatments using picosecond and femtosecond lasers have diminished material corrosion, enhancing their durability.[83] Additionally, femtosecond lasers have been employed in direct writing processes, allowing for the precise creation of complex structures ranging from 0D to 3D.[84]

In light of our current understanding, our investigation introduces a fresh perspective by unveiling a correlation between the static first hyperpolarizability of $M@b_{64/66}Al_{12}N_{12}$ and the Waber–Cromer radius of the transition metal. Furthermore, in the dynamic regime, a remarkable linear correlation exists between the first hyperpolarizability and the second hyperpolarizability.

Author contributions

Conceptualization and methodology: D. H. and H. C.; investigation: M. Z., D. H., and N. C.; writing – original draft preparation: D. H. and H. C.; writing – review & editing: M. Z., D. H., N. C. and H. C.; data curation: M. Z., D. H., N. C. and H. C. All authors have read and agreed to the published version of the manuscript.

Conflicts of interest

There are no conflicts to declare.

Acknowledgements

The authors gratefully acknowledge GENCI/IDRIS for HPC resources/computer time (Project AD010814942) and the PSMN of the ENS-Lyon for computing resources.

References

1 F. Tessore, A. O. Biroli, G. Di Carlo and M. Pizzotti, *Inorganics*, 2018, **6**, 1–17.
2 R. Bano, M. Asghar, K. Ayub, T. Mahmood and J. Iqbal, *Front. Mater.*, 2021, **8**, 1–24.
3 H. Li, H. Xu, X. Shen, K. Han, Z. Bi and R. Xu, *Sci. Rep.*, 2016, **6**, 28067.
4 P. A. Franken, A. E. Hill, C. W. Peters and G. Weinreich, *Phys. Rev. Lett.*, 1961, **7**, 118–119.
5 L. T. Cheng, W. Tam, S. R. Marder, A. E. Stiegman, G. Rikken and C. W. Spangler, *J. Phys. Chem.*, 1991, **95**, 10643–10652.
6 K. A. Green, M. P. Cifuentes, M. Samoc and M. G. Humphrey, *Coord. Chem. Rev.*, 2011, **255**, 2530–2541.
7 J. A. Delaire and K. Nakatani, *Chem. Rev.*, 2000, **100**, 1817–1845.
8 J. Dang, D. Mei, Y. Wu and Z. Lin, *Coord. Chem. Rev.*, 2021, **431**, 213692.
9 M. S. Kodikara, R. Stranger and M. G. Humphrey, *Coord. Chem. Rev.*, 2018, **375**, 389–409.
10 Y. Y. Liang, B. Li, X. Xu, F. Long Gu and C. Zhu, *J. Comput. Chem.*, 2019, **40**, 971–979.
11 N. Baggi, E. Garoni, A. Colombo, C. Dragonetti, S. Righetto, D. Roberto, J. Boixel, V. Guerchais and S. Fantacci, *Polyhedron*, 2018, **140**, 74–77.
12 C. Andraud, F. Cyril, B. Olivier, H. Chermette and P. L. Baldeck, *Adv. Polym. Sci.*, 2008, **214**, 149–203.
13 Z. R. Khan, M. Shkir, V. Ganesh, S. AlFaify, I. S. Yahia and H. Y. Zahran, *J. Electron. Mater.*, 2018, **47**, 5386–5395.
14 K. Iliopoulos, O. Krupka, D. Gindre and M. Salle, *J. Am. Chem. Soc.*, 2010, **132**, 14343–14345.

15 M. Homocianu, A. Airinei, C. Hamciuc and A. M. Ipate, *J. Mol. Liq.*, 2019, **281**, 141–149.
16 M. Blanchard-Desce, I. Ledoux, J. M. Lehn, J. Malthête and J. Zyss, *J. Chem. Soc., Chem. Commun.*, 1988, 737–739.
17 D. Hannach, N. Khelfaoui, M. Zaidi, D. Yahiaoui, S. Lakehal, C. Morell and H. Chermette, *New J. Chem.*, 2023, **47**, 1234–1246.
18 E. Cariati, C. Dragonetti, E. Lucenti, F. Nisic, S. Righetto and E. Tordin, *Chem. Commun.*, 2014, **50**, 1608–1610.
19 F. Ricci, F. Elisei, P. Foggi, A. Marrocchi, A. Spalletti and B. Carlotti, *J. Phys. Chem.*, 2016, **120**, 23726–23739.
20 F. Chérioux, H. Maillotte, P. Audebert and J. Zyss, *Chem. Commun.*, 1999, 2083–2084.
21 M. Fontani, A. Colombo, C. Dragonetti, S. Righetto, D. Roberto and D. Marinotto, *Inorganics*, 2020, **8**, 36.
22 D. Hannachi, M. F. Haroun, A. Khireddine and H. Chermette, *New J. Chem.*, 2019, **43**, 14377.
23 M. Zaidi, D. Hannachi and H. Chermette, *Inorg. Chem.*, 2021, **60**, 6616–6632.
24 D. Kamli, D. Hannachi, D. Samsar and H. Chermette, *New J. Chem.*, 2023, **47**, 1234–1246.
25 A. Ahsin and K. Ayub, *J. Nanostruct. Chem.*, 2022, **12**, 529–545.
26 A. Ahsan and K. Ayub, *Opt. Laser Technol.*, 2020, **129**, 106298.
27 A. Ahsan, S. Sarfaraz, F. Fayyaz, M. Asghar and K. Ayub, *J. Mol. Liq.*, 2022, **350**, 118504.
28 A. Ahsan and K. Ayub, *J. Mol. Liq.*, 2020, **297**, 36–40.
29 S. J. Wang, Y. F. Wang and C. Cai, *J. Phys. Chem. C*, 2015, **119**, 16256–16262.
30 S. J. Wang, Y. F. Wang and C. Cai, *J. Phys. Chem. C*, 2015, **119**, 5589–5595.
31 B. Ni, W. Sun, J. Kang and Y. Zhang, *J. Phys. Chem. C*, 2020, **124**, 11595–11608.
32 D. Paul, J. Deb and U. Sarkar, *ChemistrySelect*, 2020, **5**, 6987–6999.
33 F. Khaliq, T. Mahmood, K. Ayub, S. Tabassum and M. Amjad, *Polyhedron*, 2021, **200**, 115145.
34 Y. Arshad, M. Asghar, M. Yar, T. Bibi and K. Ayub, *J. Inorg. Organomet. Polym. Mater.*, 2023, **33**, 943–955.
35 K. A. Faizan Ullah, N. Kosar, A. Ali, Maria and T. Mahmood, *Opt. - Int. J. Light Electron Opt.*, 2019, **207**, 163792.
36 H. Wu, F. Zhang, X. Xu, C. Zhang and H. Jiao, *J. Phys. Chem. A*, 2003, **107**, 204–209.
37 M. Niu, G. Yu, G. Yang, W. Chen, X. Zhao and X. Huang, *Inorg. Chem.*, 2014, **53**, 349–358.
38 E. Shakerzdeh, E. Tahmasebi and H. R. Shamlouei, *Synth. Met.*, 2015, **204**, 17–24.
39 E. Shakerzadeh, E. Tahmasebi and Z. Biglari, *J. Mol. Liq.*, 2016, **221**, 443–451.
40 E. Tahmasebi, E. Shakerzadeh and Z. Biglari, *Appl. Surf. Sci.*, 2016, **363**, 197–208.
41 M. A. Gilani, S. Tabassum, U. Gul, T. Mahmood, A. I. Alharthi, M. A. Alotaibi, M. Geesi, R. Sheikh and K. Ayub, *Appl. Phys. A: Mater. Sci. Process.*, 2018, **124**, 14.
42 Y. Arshad, S. Khan, M. A. Hashmi and K. Ayub, *New J. Chem.*, 2018, **42**, 6976–6989.
43 S. Irshad, F. Ullah, S. Khan, R. Ludwig and T. Mahmood, *Opt. Laser Technol. J.*, 2021, **134**, 106570.
44 M. J. Frisch, G. W. Trucks, H. B. Schlegel, G. E. Scuseria, M. A. Robb, J. R. Cheeseman, G. Scalmani, V. Barone, G. A. Petersson, H. Nakatsuji, X. Li, M. Caricato, A. V. Marenich, J. Bloino, B. G. Janesko, R. Gomperts, B. Mennucci, H. P. Hratchian, J. V. Ortiz, A. F. Izmaylov, J. L. Sonnenberg, D. Williams-Young, F. Ding, F. Lipparini, F. Egidi, J. Goings, B. Peng, A. Petrone, T. Henderson, D. Ranasinghe, V. G. Zakrzewski, J. Gao, N. Rega, G. Zheng, W. Liang, M. Hada, M. Ehara, K. Toyota, R. Fukuda, J. Hasegawa, M. Ishida, T. Nakajima, Y. Honda, O. Kitao, H. Nakai, T. Vreven, K. Throssell, J. A. Montgomery Jr., J. E. Peralta, F. Ogliaro, M. J. Bearpark, J. J. Heyd, E. N. Brothers, K. N. Kudin, V. N. Staroverov, T. A. Keith, R. Kobayashi, J. Normand, K. Raghavachari, A. P. Rendell, J. C. Burant, S. S. Iyengar, J. Tomasi, M. Cossi, J. M. Millam, M. Klene, C. Adamo, R. Cammi, J. W. Ochterski, R. L. Martin, K. Morokuma, O. Farkas, J. B. Foresman and D. J. Fox, *Gaussian 16, Revision A.03*, Gaussian, Inc., Wallin, 2016.
45 T. Yanai, D. P. Tew and N. C. Handy, *Chem. Phys. Lett.*, 2004, **393**, 51–57.
46 R. F. W. Bader, T. T. Nguyen-Dang and Y. Tal, *J. Chem. Phys.*, 1979, **70**, 4316–4329.
47 R. F. W. Bader, *Chem. Rev.*, 1991, **91**, 893–928.
48 R. F. W. Bader, *Acc. Chem.*, 1985, **18**, 9–15.
49 P. S. V. Kumar, V. Raghavendra and V. Subramanian, *J. Chem. Sci.*, 2016, **128**, 1527–1536.
50 H. A. Kurtz, J. J. P. Stewart and K. M. Dieter, *J. Comput. Chem.*, 1990, **11**, 82–87.
51 D. P. Shelton and J. E. Rice, *Chem. Rev.*, 1994, **94**, 3–29.
52 A. Plaquet, M. Guillaume, B. Champagne, F. Castet, L. Ducasse, J. L. Pozzo and V. Rodriguez, *Phys. Chem. Chem. Phys.*, 2008, **10**, 6223–6232.
53 N. Hou, R. Feng and X. H. Fang, *Int. J. Quantum Chem.*, 2022, **122**, 1–14.
54 M. Chołuj, M. M. Alam, M. T. P. Beerepoot, S. P. Sitkiewicz, E. Matito, K. Ruud and R. Zaleśny, *J. Chem. Theory Comput.*, 2022, **18**, 1046–1060.
55 P. Besalú-Sala, S. P. Sitkiewicz, P. Salvador, E. Matito and J. M. Luis, *Phys. Chem. Chem. Phys.*, 2020, **22**, 11871–11880.
56 D. Grabarek and T. Andruniów, *J. Chem. Theory Comput.*, 2019, **15**, 490–508.
57 Maria, J. Iqbal and K. Ayub, *RSC Adv.*, 2016, **6**, 94228–94235.
58 S. Sarwar, J. Yaqoob, M. U. Khan, R. Hussain, S. Zulfiqar, A. Anwar, M. A. Assiri, M. Imran, M. M. Ibrahim, G. A. M. Mersal and A. Y. Elnaggar, *ACS Omega*, 2022, **7**, 24396–24414.
59 L. M. G. Abegaõ, R. D. Fonseca, F. A. Santos, J. J. Rodrigues, K. Kamada, C. R. Mendonca, S. Piguel and L. De Boni, *RSC Adv*, 2019, **9**, 26476–26482.
60 H. M. He, H. Yang, Y. Li and Z. R. Li, *Front. Chem.*, 2022, **10**, 1–10.
61 L. Lescos, S. P. Sitkiewicz, P. Beaujean, M. Blanchard-Desce, B. Champagne, E. Matito and F. Castet, *Phys. Chem. Chem. Phys.*, 2020, **22**, 16579–16594.

62 T. Lu and F. Chen, *J. Comput. Chem.*, 2012, **33**, 580–592.
63 Z. Liu, T. Lu, Q. Chen, T. Lu and Q. Chen, *Carbon N. Y.*, 2020, **165**, 461–467.
64 D. Hannachi, N. Ouddai, M. Arotçaréna and H. Chermette, *Mol. Phys.*, 2015, **113**, 1541–1550.
65 G. te Velde, F. M. Bickelhaupt, E. J. Baerends, C. Fonseca Guerra, S. J. A. van Gisbergen, J. G. Snijders and T. Ziegler, *J. Comput. Chem.*, 2001, **22**, 931–967.
66 E. J. Baerends, T. Ziegler, A. J. Atkins, J. Autschbach, D. Bashford, A. Bérces, F. M. Bickelhaupt, C. Bo, P. M. Boerrigter, L. Cavallo, D. P. Chong, D. V. Chul-hai, L. Deng, R. M. Dickson, J. M. Dieterich, D. E. Ellis, M. van Faassen, L. Fan, T. H. Fischer, C. Fonseca Guerra, M. Franchini, A. Ghysels, A. Giammona, S. J. A. van Gisbergen, A. W. Götz, J. A. Groeneveld, O. V. Gritsenko, M. Grüning, S. Gusarov, F. E. Harris, P. van den Hoek, C. R. Jacob, H. Jacobsen, L. Jensen, J. W. Kaminski, G. van Kessel, F. Kootstra, A. Kovalenko, M. V. Krykunov, E. van Lenthe, D. A. McCormack, A. Michalak, M. Mitoraj, S. M. Morton, J. Neugebauer, V. P. Nicu, L. Noodleman, V. P. Osinga, S. Patchkovskii, M. Pavanello, C. A. Peeples, P. H. T. Philipsen, D. Post, C. C. Pye, W. Ravenek, J. I. Rodriguez, P. Ros, R. Rüger, P. R. T. Schipper, H. van Schoot, G. Schreckenbach, J. S. Seldenthuis, M. Seth, J. G. Snijders, M. Solà, M. Swart, D. Swerhone, G. te Velde, P. Vernooijs, L. Ver-sluis, L. Visscher, O. Visser, F. Wang, T. A. Wesolowski, E. M. van Wezenbeek, G. Wiesenekker, S. K. Wolff, T. K. Woo and A. L. Yakovlev, *ADF2016.01, SCM, Theoretical Chemistry*, Vrije Universiteit, Amsterdam, The Netherlands, 2016, (**http://www.Scm.Com**).
67 E. Espinosa, I. Alkorta, J. Elguero and E. Molins, *J. Chem. Phys.*, 2002, **117**, 5529–5542.
68 R. F. W. Bader, A. Streitwieser, A. Neuhaus, K. E. Laidig and P. Speers, *J. Am. Chem. Soc.*, 1996, **118**, 4959–4965.
69 X. Fradera, M. A. Austen and R. F. W. Bader, *J. Phys. Chem. A*, 1999, **103**, 304–314.
70 L. J. Farrugia, C. Evans, H. M. Senn, M. M. Hänninen and R. Sillanpää, *Organometallics*, 2012, **31**, 2559–2570.
71 R. Arun Kumar, M. Arivanandhan and Y. Hayakawa, *Prog. Cryst. Growth Charact. Mater.*, 2013, **59**, 113–132.
72 F. Ullah, N. Kosar, K. Ayub, M. A. Gilani and T. Mahmood, *New J. Chem.*, 2019, **43**, 5727–5736.
73 C. C. Yang, L. Li, W. Q. Tian, W. Q. Li and L. Yang, *Phys. Chem. Chem. Phys.*, 2022, **24**, 13275–13285.
74 U. Hohm and A. J. Thakkar, *J. Phys. Chem. A*, 2012, **116**, 697–703.
75 Z. Liu, T. Lu and Q. Chen, *Carbon*, 2020, **165**, 461–467.
76 N. Kosar, S. Wajid, K. Ayub and A. Mahmood, *Optik*, 2023, **276**, 170660.
77 C. Brée, A. Demircan and G. Steinmeyer, *IEEE J. Quantum Electron.*, 2010, **46**, 433–437.
78 M. Tarazkar, D. A. Romanov and R. J. Levis, *J. Chem. Phys.*, 2014, **140**, 214316.
79 J. L. Oudar and D. S. Chemla, *J. Chem. Phys.*, 1976, **66**, 2664–2668.
80 J. L. Oudar, *J. Chem. Phys.*, 1977, **67**, 446–457.
81 R. A. Rajan, C. V. Ngo, J. Yang, Y. Liu, K. S. Rao and C. Guo, *Opt. Laser Technol.*, 2021, **143**, 107241.
82 K. Sugioka, *Nanophotonics*, 2017, **6**, 393–413.
83 P. Pou-Álvarez, A. Riveiro, X. R. Nóvoa, M. Fernández-Arias, J. del Val, R. Comesaña, M. Boutinguiza, F. Lusquiños and J. Pou, *Surf. Coatings Technol.*, 2021, **427**, 127802.
84 R. Kurimoto, E. Niiyama and M. Ebara, *Fibrous Materials*, Elsevier Inc., 2016.

